



UNIVERSITY OF LEEDS

This is a repository copy of *Iron(II) Complexes of 4-(Alkyldisulfanyl)-2,6-di(pyrazolyl)pyridine Derivatives. Correlation of Spin-Crossover Cooperativity with Molecular Structure Following Single-Crystal-to-Single-Crystal Desolvation.*

White Rose Research Online URL for this paper:

<https://eprints.whiterose.ac.uk/183263/>

Version: Accepted Version

Article:

Kulmaczewski, R, Kershaw Cook, LJ, Pask, CM orcid.org/0000-0002-2241-5069 et al. (2 more authors) (2022) Iron(II) Complexes of 4-(Alkyldisulfanyl)-2,6-di(pyrazolyl)pyridine Derivatives. Correlation of Spin-Crossover Cooperativity with Molecular Structure Following Single-Crystal-to-Single-Crystal Desolvation. *Crystal Growth and Design*, 22 (3). pp. 1960-1971. ISSN 1528-7483

<https://doi.org/10.1021/acs.cgd.2c00005>

© 2022 American Chemical Society. This is an author produced version of an article, published in *Crystal Growth and Design*. Uploaded in accordance with the publisher's self-archiving policy.

Reuse

Items deposited in White Rose Research Online are protected by copyright, with all rights reserved unless indicated otherwise. They may be downloaded and/or printed for private study, or other acts as permitted by national copyright laws. The publisher or other rights holders may allow further reproduction and re-use of the full text version. This is indicated by the licence information on the White Rose Research Online record for the item.

Takedown

If you consider content in White Rose Research Online to be in breach of UK law, please notify us by emailing eprints@whiterose.ac.uk including the URL of the record and the reason for the withdrawal request.



eprints@whiterose.ac.uk
<https://eprints.whiterose.ac.uk/>

Iron(II) Complexes of 4-(Alkyldisulfanyl)-2,6-di(pyrazolyl)pyridine Derivatives. Correlation of Spin-Crossover Cooperativity with Molecular Structure Following Single-Crystal-to-Single-Crystal Desolvation

Rafal Kulmaczewski,[†] Laurence J. Kershaw Cook,^{†,¶} Christopher M. Pask,[†] Oscar Cespedes[‡] and Malcolm A. Halcrow^{†*}

[†]School of Chemistry, University of Leeds, Woodhouse Lane, Leeds LS2 9JT, UK. Email: m.a.halcrow@leeds.ac.uk.

[‡]School of Physics and Astronomy, University of Leeds, E. C. Stoner Building, Leeds LS2 9JT, UK.

ABSTRACT: The complex salts $[\text{Fe}(L^1)_2]\text{X}_2$ ($\mathbf{1X}_2$; $L^1 = 4$ -(*iso*propyl)disulfanyl)-2,6-di(pyrazolyl)pyridine; $\text{X}^- = \text{BF}_4^-$ or ClO_4^-) form solvated crystals from common organic solvents. Crystals of $\mathbf{1X}_2 \cdot \text{Me}_2\text{CO}$ show abrupt spin-transitions near 160 K, with up to 22 K thermal hysteresis. $\mathbf{1X}_2 \cdot \text{Me}_2\text{CO}$ co-crystallizes with other, less cooperative acetone solvates, which all transform into the same solvent-free materials $\mathbf{1X}_2 \cdot \text{sf}$ upon exposure to air, or mild heating. Conversion of $\mathbf{1X}_2 \cdot \text{Me}_2\text{CO}$ to $\mathbf{1X}_2 \cdot \text{sf}$ proceeds in single-crystal-to-single-crystal fashion. $\mathbf{1X}_2 \cdot \text{sf}$ are not isomorphous with the acetone solvates, and exhibit abrupt spin-transitions at low temperature with hysteresis loops of 30–38 K ($\text{X}^- = \text{BF}_4^-$) and 10–20 K ($\text{X}^- = \text{ClO}_4^-$), depending on the measurement method. Interestingly, the desolvation has an opposite effect on the SCO temperature and hysteresis in the two salts. The hysteretic spin-transitions in $\mathbf{1X}_2 \cdot \text{Me}_2\text{CO}$ and $\mathbf{1X}_2 \cdot \text{sf}$ do not involve a crystallographic phase change, but are accompanied by a significant rearrangement of the metal coordination sphere. Other solvates $\mathbf{1X}_2 \cdot \text{MeNO}_2$, $\mathbf{1X}_2 \cdot \text{MeCN}$ and $\mathbf{1X}_2 \cdot \text{H}_2\text{O}$ are mostly isomorphous with each other, and show more gradual spin-crossover equilibria near room temperature. All three of these lattice types have similar unit cell dimensions, and contain cations associated into chains through pairwise, intermolecular $\text{S} \cdots \pi$ interactions. Polycrystalline $[\text{Fe}(L^2)_2][\text{BF}_4]_2 \cdot \text{MeNO}_2$ ($2[\text{BF}_4]_2 \cdot \text{MeNO}_2$; $L^2 = 4$ -(methyl)disulfanyl)-2,6-di(pyrazolyl)pyridine) shows an abrupt spin-transition just above room temperature, with an unsymmetric and structured hysteresis loop, whose main features are reversible upon repeated thermal scanning.

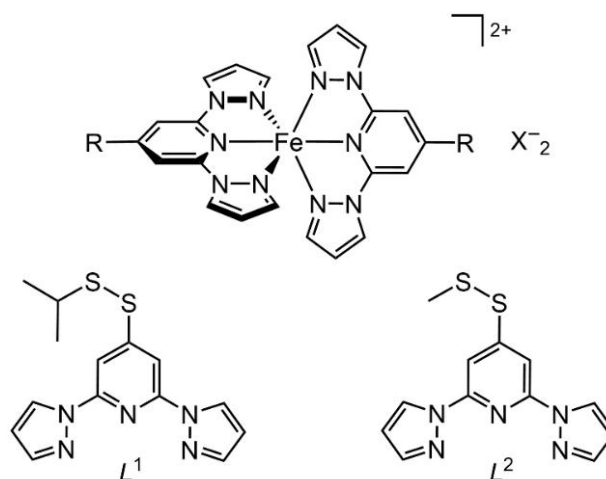
Introduction

Crystal engineering of metal/organic spin-crossover (SCO) materials^{1–7} involves the interplay between the individual molecular switching centers, and their surrounding lattice.⁸ The cooperativity of spin-crossover reflects the structural changes occurring during the transition. That is, greater structural changes between the high-spin and low-spin forms lead to abrupt and/or hysteretic spin-transitions, and *vice versa*.⁹ SCO materials which are isomorphous, or exhibit variations of the same packing motif, are particularly helpful in allow small differences between materials to be correlated with their switching function within the same lattice environment.^{10–20}

Cooperative spin-transitions often involve a crystallographic phase change,^{21,22} but wide hysteresis can arise without a phase change if the complex undergoes a large, anisotropic structural rearrangement between its spin states.^{23–26} However, to complicate matters, SCO may not occur if the structural difference between the spin states is too great, or if the crystal is too densely packed.^{9,27,28} Both scenarios increase the activation energy of SCO so it becomes quenched on kinetic grounds, even where a compound exhibits SCO under other conditions, such as in solution.²⁹ Cooperative SCO requires a balanced combination of structural factors that are not too large, but not too small.

Derivatives of $[\text{Fe}(\text{bpp})_2]^{2+}$ ($\text{bpp} = 2,6$ -di{pyrazol-1-yl}pyridine; Chart 1) can be prepared with a variety of pyridyl and/or pyrazolyl substituents, which often exhibit SCO at accessible temperatures.^{27,28,30,31} The library of $[\text{Fe}(\text{bpp}^R)_2]\text{X}_2$ (X^- = a monovalent anion) compounds is now large enough to allow

Chart 1 Top: the structure of $[\text{Fe}(\text{bpp}^R)_2]^{2+}$ (the parent complex $[\text{Fe}(\text{bpp})_2]^{2+}$ has $\text{R} = \text{H}$). **Bottom:** the two new bpp^R derivatives described in this work.



structure: function correlations to be derived.^{32,33} Iron complexes of 4-alkylsulfanyl-2,6-di{pyrazol-1-yl}pyridine ligands (bpp^R , $\text{R} = \text{SMe}$, SiPr or SiBu) have been particularly useful.^{19,34–38} For example, solvate crystals of formula $[\text{Fe}(\text{bpp}^{\text{SiPr}})_2]\text{X}_2 \cdot \text{solv}$ ($\text{X}^- = \text{BF}_4^-$ or ClO_4^- ; $\text{solv} = \text{MeCN}$, EtCN , MeNO_2 , Me_2CO , H_2O or sf {solvent-free}) are all isomorphous in both spin states, and can be interconverted by single-crystal-to-single-crystal solvent exchange. These exhibit a variety of

spin state behaviors that correlate with the shape of the lattice solvent molecule.^{19,36,37}

The bpp^{SMe} and bpp^{SiPr} ligands in these studies were synthesized by alkylation of 4-mercapto-2,6-di{pyrazol-1-yl}pyridine (bpp^{SH}) with the appropriate iodoalkane.^{34,36,39} Since the product mixtures from these reactions contained lower yields of the corresponding 4-alkyldisulfanyl-substituted byproducts, we decided to investigate the iron complex chemistry of those ligands, as well. We report here a family of SCO-active solvate crystals $[\text{Fe}(L^1)_2]X_2$ ($\mathbf{1X}_2$; $L^1 = 4\text{-isopropylidysulfanyl-2,6-di}\{\text{pyrazol-1-yl}\}\text{pyridine}$; $X^- = \text{BF}_4^-$ or ClO_4^- ; Scheme 1). Many of these solvates show clear structural similarities, which can be correlated with their SCO characteristics. Moreover, annealing some solvates causes single-crystal-to-single-crystal conversion to a solvent-free phase,^{40,41} showing a hysteretic spin-transition that we have fully structurally characterized. A solvate of $[\text{Fe}(L^2)_2][\text{BF}_4]_2$ ($\mathbf{2}[\text{BF}_4]_2$; $L^2 = 4\text{-methylidysulfanyl-2,6-di}\{\text{pyrazol-1-yl}\}\text{pyridine}$) showing an unusual asymmetric spin-transition profile is also briefly presented.

Experimental

The synthetic protocol and characterization data for L^1 are given in the Supporting Information. The synthesis of L^2 followed our published method.²⁶ Unless otherwise stated, reagents and solvents were purchased commercially and used as supplied.

Caution. Although we have experienced no problems when using the perchlorate salts in this study, metal-organic perchlorates are potentially explosive and should be handled with care in small quantities.

Synthesis of $[\text{Fe}(L^1)_2][\text{BF}_4]_2$ ($\mathbf{1}[\text{BF}_4]_2$). A mixture of L^1 (50 mg, 0.16 mmol) and $\text{Fe}[\text{BF}_4]_2 \cdot 6\text{H}_2\text{O}$ (27 mg, 0.080 mmol) in nitromethane (10 cm^3) was stirred at room temperature until all the solid had dissolved. The orange solution was filtered, and the complex was precipitated by dropwise addition of diethyl ether (50 cm^3). The orange powder was collected on a glass frit and washed with diethyl ether. Yield 44 mg, 64 %.

Solvate crystals of the complex were obtained by recrystallizing the crude powder from acetone, acetonitrile or nitromethane by diethyl ether vapor diffusion. Monohydrate crystals of the complexes were produced similarly, from undried methanol solutions. The lattice solvent in the organic solvate crystals is replaced by atmospheric moisture upon exposure to air. Most microanalyses from samples of these materials were approximately consistent with a sesquihydrate formulation. Found: C, 37.6; H, 3.48; N, 15.5 %. Calcd for $\text{C}_{28}\text{H}_{30}\text{B}_2\text{F}_8\text{FeN}_{10}\text{S}_4 \cdot 1.5\text{H}_2\text{O}$: C, 37.7; H, 3.73; N, 15.7 %. ^1H NMR (CD_3NO_2) δ 1.2 (12H, $\text{SCH}\{\text{CH}_3\}_2$), 3.1 (2H, $\text{SCH}\{\text{CH}_3\}_2$), 40.2 (4H, Py $H^{3/5}$), 40.6 (4H, Pz H^5), 59.3 (4H, Pz H^4), 68.4 (4H, Pz H^3).

A good microanalysis was obtained from one organic solvate formulation, produced by recrystallization from acetone/diethyl ether. Found: C, 40.8; H, 4.00; N, 14.9 %. Calcd for $\text{C}_{28}\text{H}_{30}\text{B}_2\text{F}_8\text{FeN}_{10}\text{S}_4 \cdot \text{C}_3\text{H}_6\text{O}$: C, 40.4; H, 3.93; N, 15.2 %.

Synthesis of $[\text{Fe}(L^1)_2][\text{ClO}_4]_2$ ($\mathbf{1}[\text{ClO}_4]_2$). Method as for $\mathbf{1}[\text{BF}_4]_2$, using $\text{Fe}[\text{ClO}_4]_2 \cdot 6\text{H}_2\text{O}$ (29 mg, 0.080 mmol). The product was an orange powder. Yield 51 mg, 72 %.

Solvate crystals of $\mathbf{1}[\text{ClO}_4]_2$ were produced as above, and were similarly sensitive to solvent loss in air. Most samples of $\mathbf{1}[\text{ClO}_4]_2$ also analyzed to a sesquihydrate formulation. Found: C, 36.7; H, 3.40; N, 15.4 %. Calcd for $\text{C}_{28}\text{H}_{30}\text{B}_2\text{F}_8\text{FeN}_{10}\text{S}_4 \cdot 1.5\text{H}_2\text{O}$: C, 36.7; H, 3.63; N, 15.3 %.

A good microanalysis was obtained from a solvent-free sample, produced by annealing a mixture of acetone solvate crystals at 370 K. Found: C, 37.6; H, 3.47; N, 15.4 %. Calcd for $\text{C}_{28}\text{H}_{30}\text{Cl}_2\text{FeN}_{10}\text{O}_8\text{S}_4$: C, 37.8; H, 3.40; N, 15.7 %.

Synthesis of $[\text{Fe}(L^2)_2][\text{BF}_4]_2$ ($\mathbf{2}[\text{BF}_4]_2$). Method as above, using L^2 (47 mg, 0.16 mmol). The product was an orange powder, which formed brown single crystals when recrystallized from MeCN or MeNO₂ solution with a diethyl ether vapor. The crystals decomposed to a solvent-free powder on drying *in vacuo*. Yield 57 mg, 88 %. Found: C, 35.3; H, 2.80; N, 17.3 %. Calcd for $\text{C}_{24}\text{H}_{22}\text{B}_2\text{F}_8\text{FeN}_{10}\text{S}_4$: C, 35.7; H, 2.74; N, 17.3 %. ^1H NMR (CD_3NO_2) δ 2.5 (6H, SCH_3), 39.6 (4H, Py $H^{3/5}$), 40.2 (4H, Pz H^5), 58.6 (4H, Pz H^4), 68.5 (4H, Pz H^3).

Single crystal X-ray structure analyses

Crystals of L^1 were obtained upon slow evaporation of an NMR sample of that compound in CDCl_3 . Crystals of each $\mathbf{1}[\text{BF}_4]_2$ -solv, $\mathbf{1}[\text{ClO}_4]_2$ -solv and $\mathbf{2}[\text{BF}_4]_2$ -solv material were prepared as described above. The $\mathbf{1X}_2$ -sf ($X^- = \text{BF}_4^-$ and ClO_4^-) crystals were obtained by annealing crystals of $\mathbf{1X}_2 \cdot \text{Me}_2\text{CO}$ on the diffractometer at 370 K for 30 mins. Where relevant, the same crystal was used for data collections at multiple temperatures.

All diffraction data were collected with an Agilent Supernova dual source diffractometer using monochromated Cu- K_α radiation ($\lambda = 1.54184 \text{ \AA}$). Experimental details of each structure determination, and full details of all the crystallographic refinements, are given in the Supporting Information (Table S1). The structures were solved by direct methods (*SHELXS*), and developed by full least-squares refinement on F^2 (*SHELXL-2018*).⁴² Crystallographic figures were prepared using *X-SEED*,⁴³ and structural parameters tabulated in the Supporting Information were calculated with *Olex 2*.⁴⁴ Hirshfeld surface calculations were performed with *CrystalExplorer*.⁴⁵

Other measurements

Elemental analyses were performed by the microanalytical services at the University of Leeds School of Chemistry, or London Metropolitan University School of Human Sciences. Electrospray mass spectra were recorded on a Bruker Micro-TOF-q instrument from CHCl_3 solution. Diamagnetic NMR spectra employed a Bruker AV3HD spectrometer operating at 400.1 (^1H) or 100.6 MHz (^{13}C), while paramagnetic ^1H NMR spectra were obtained with a Bruker AV3 spectrometer operating at 300.1 MHz. X-ray powder diffraction data were measured at 298 K with a Bruker D2 Phaser diffractometer, using Cu- K_α radiation ($\lambda = 1.5419 \text{ \AA}$). Some powder diffraction samples were coated in nujol to protect against solvent loss during measurement; details are in the Supporting Information. Thermogravimetric analyses were obtained with a TA Instruments TGA Q50 analyser heating at a rate of 10 K min^{-1} under a stream of nitrogen gas.

Magnetic susceptibility measurements were performed using a Quantum Design MPMS-3 VSM magnetometer, in an applied field of 5000 G. Unless otherwise stated, samples were measured at a scan rate of 5 K min^{-1} . Diamagnetic corrections for the samples were estimated from Pascal's constants;⁴⁶ a diamagnetic correction for the sample holder was also applied to the data. Samples were protected against solvent loss by saturating the tightly sealed MPMS-3 powder capsules with diethyl ether

vapor, although the acetone solvates often desolvated rapidly *in situ* despite that precaution (Figure S25).

Susceptibility measurements in solution were obtained by Evans method using a Bruker AV-NEO spectrometer operating at 500.2 MHz.⁴⁷ A diamagnetic correction for the sample,⁴⁶ and a correction for the variation of the density of the CD₃CN solvent with temperature,⁴⁸ were applied to these data.

Results and Discussion

Reaction of bpp^{SH} ⁴⁹ with 2-iodopropane or iodomethane in refluxing acetonitrile, in the presence of potassium carbonate, affords a mixture including bpp^{SR} ($\text{R}^{\cdot} = \text{Me}$ or $i\text{Pr}$), bpp^{SSR} (*ie* L^1 or L^2 ; Scheme 1) and *bis*{2,6-di{pyrazol-1-yl}pyrid-4-yl}disulfide. These were separated by a sequence of precipitation and chromatography steps, from which L^1 and L^2 can be isolated in 20-30 % yield. We obtained a significant quantity of L^1 during our studies of the $[\text{Fe}(\text{bpp}^{\text{SPR}})_2]\text{X}_2\cdot\text{solv}$ system,^{19,36,37} allowing us to investigate its iron chemistry in detail. Since L^2 was only available in smaller amounts, however, fewer experiments were undertaken with that ligand.³⁴

The complex salts $\mathbf{1}[\text{BF}_4]_2$, $\mathbf{1}[\text{ClO}_4]_2$ and $\mathbf{2}[\text{BF}_4]_2$ were obtained by treatment of $\text{Fe}[\text{BF}_4]_2\cdot 6\text{H}_2\text{O}$ or $\text{Fe}[\text{ClO}_4]_2\cdot 6\text{H}_2\text{O}$ with two equiv of the appropriate ligand in nitromethane. Addition of excess diethyl ether afforded the complexes as orange powders, which were recrystallized from different organic solvents by diethyl ether vapor diffusion. Dried polycrystalline $\mathbf{1}[\text{BF}_4]_2$ and $\mathbf{1}[\text{ClO}_4]_2$ readily absorb atmospheric moisture, and consistently analyzed to the formulations $\mathbf{1}[\text{BF}_4]_2\cdot 1.5\text{H}_2\text{O}$ and $\mathbf{1}[\text{ClO}_4]_2\cdot 1.5\text{H}_2\text{O}$. Dried samples of $\mathbf{2}[\text{BF}_4]_2$ were solvent-free by elemental analysis.

Recrystallization of $\mathbf{1}[\text{BF}_4]_2$ and $\mathbf{1}[\text{ClO}_4]_2$ from acetone/ diethyl ether yielded mixtures of crystal phases, which could be distinguished by their color and morphology. These included yellow needles of composition $\mathbf{1}\text{X}_2\cdot \text{Me}_2\text{CO}$ ($\text{X}^- = \text{BF}_4^-$ or ClO_4^- ; monoclinic, space group $P2_1/c$, $Z = 4$), whose metric parameters show they are high-spin at 250 K but low-spin at 143 K ($\text{X}^- = \text{BF}_4^-$) or 100 K ($\text{X}^- = \text{ClO}_4^-$). Variable temperature unit cell data confirm both crystals undergo abrupt spin-transitions near 150 K, with a 10 K thermal hysteresis being measured for the perchlorate salt (Table 1, Figures S7-S10).⁵⁰

The solvate $\mathbf{1}[\text{BF}_4]_2\cdot \text{Me}_2\text{CO}$ co-crystallized with two brown pseudopolymorphs with needle and prismatic morphologies, with the respective formulae $\mathbf{1}[\text{BF}_4]_2\cdot 0.75\text{Me}_2\text{CO}$ (triclinic, $P\bar{1}$, $Z = 4$) and $\mathbf{1}[\text{BF}_4]_2\cdot 0.5\text{Me}_2\text{CO}\cdot 0.5\text{H}_2\text{O}$ (monoclinic, $P2_1/c$, $Z = 8$). Both these solvates contain two unique complex molecules per asymmetric unit. Molecule A of $\mathbf{1}[\text{BF}_4]_2\cdot 0.75\text{Me}_2\text{CO}$ is low-spin while molecule B is high-spin at 250 K. However, at 120 K molecule B exhibits whole-ligand disorder implying a *ca* 3:1 high:low-spin population, which indicates the onset of SCO at that temperature. In contrast, both cation environments in $\mathbf{1}[\text{BF}_4]_2\cdot 0.5\text{Me}_2\text{CO}\cdot 0.5\text{H}_2\text{O}$ are low-spin at both 120 and 250 K.

One brown single crystalline contaminant was noted in samples of $\mathbf{1}[\text{ClO}_4]_2\cdot \text{Me}_2\text{CO}$, namely $\mathbf{1}[\text{ClO}_4]_2\cdot m\text{Me}_2\text{CO}\cdot 0.5\text{H}_2\text{O}$ ($m \approx 0.34$; monoclinic, $P2_1/c$, $Z = 8$). This is not isomorphous with $\mathbf{1}[\text{BF}_4]_2\cdot 0.5\text{Me}_2\text{CO}\cdot 0.5\text{H}_2\text{O}$, but like that compound $\mathbf{1}[\text{ClO}_4]_2\cdot m\text{Me}_2\text{CO}\cdot 0.5\text{H}_2\text{O}$ is fully low-spin at 120 K (an attempted measurement at higher temperature led to crystal decomposition). A residual low-temperature paramagnetism in fresh samples of ' $\mathbf{1}[\text{ClO}_4]_2\cdot x\text{Me}_2\text{CO}$ ' (see below) implies a third phase may also be present in those samples, but it was not isolated as a pure (poly)crystalline material.

Table 1. Summary of the solvate crystal phases obtained in this work, and their spin state properties.

| Phase | Spin state properties, $T_{1/2}$ (K) |
|---|--|
| $\mathbf{1}[\text{BF}_4]_2\cdot \text{Me}_2\text{CO}$ | $T_{1/2\downarrow} = 175\pm 5$, $T_{1/2\uparrow} = 175\pm 5^{\text{a,b}}$ |
| $\mathbf{1}[\text{ClO}_4]_2\cdot \text{Me}_2\text{CO}$ | $T_{1/2\downarrow} = 155\pm 5$, $T_{1/2\uparrow} = 165\pm 5^{\text{a}}$ $T_{1/2\downarrow} = 151$, $T_{1/2\uparrow} = 173^{\text{d}}$ |
| $\mathbf{1}[\text{BF}_4]_2\cdot 0.75\text{Me}_2\text{CO}$ | 1:1 low:high-spin at 250 K ^a |
| $\mathbf{1}[\text{BF}_4]_2\cdot 0.5\text{Me}_2\text{CO}\cdot 0.5\text{H}_2\text{O}$ | Low-spin at $T \leq 250$ K ^a |
| $\mathbf{1}[\text{ClO}_4]_2\cdot m\text{Me}_2\text{CO}\cdot 0.5\text{H}_2\text{O}$ | Gradual SCO; $T_{1/2} = 325\pm 2^{\text{c}}$ |
| $\mathbf{1}[\text{BF}_4]_2\cdot \text{MeNO}_2$ | Gradual SCO; $T_{1/2} = 270^{\text{c}}$ |
| $\mathbf{1}[\text{ClO}_4]_2\cdot n\text{MeNO}_2$ | Gradual SCO; $T_{1/2} = 264^{\text{c}}$ |
| $\mathbf{1}[\text{BF}_4]_2\cdot \text{MeCN}$ | Gradual SCO; $T_{1/2} = 316^{\text{d}}$ |
| $\mathbf{1}[\text{ClO}_4]_2\cdot \text{MeCN}$ | Gradual SCO; $T_{1/2} = 299^{\text{c,d}}$ |
| $\mathbf{1}[\text{BF}_4]_2\cdot \text{H}_2\text{O}$ | Gradual SCO; $T_{1/2} = 342^{\text{c}}$ |
| $\mathbf{1}[\text{ClO}_4]_2\cdot \text{H}_2\text{O}$ | Gradual SCO; $T_{1/2} = 321^{\text{c}}$ |
| $\mathbf{1}[\text{BF}_4]_2\cdot \text{sf}$ | $T_{1/2\downarrow} = 127.5\pm 2.5$, $T_{1/2\uparrow} = 165\pm 5^{\text{a}}$ $T_{1/2\downarrow} = 135$, $T_{1/2\uparrow} = 159^{\text{c,e}}$ |
| $\mathbf{1}[\text{ClO}_4]_2\cdot \text{sf}$ | $T_{1/2\downarrow} = 165\pm 5$, $T_{1/2\uparrow} = 185\pm 5^{\text{a}}$ $T_{1/2\downarrow} = 174$, $T_{1/2\uparrow} = 184^{\text{c}}$ |

^aFrom crystallographic data. ^bA magnetic measurement of this transition from a phase-pure sample was not achieved. See also ref. 50. ^cFrom magnetic susceptibility data. ^dThese magnetic data are inconsistent with the crystal structure of this compound. See the text for more details. ^eSCO is incomplete in the magnetic measurements, because a fraction of the sample is kinetically trapped in its high-spin state below the transition temperature.

The acetone solvate crystals of $\mathbf{1}[\text{BF}_4]_2$ and $\mathbf{1}[\text{ClO}_4]_2$ were manually separated for characterization by X-ray powder diffraction (Figures S20-S21). Those samples were each phase-pure, implying there were no other uncharacterized materials in the mixtures. However, useful powder patterns were only obtained if the samples were coated with nujol, to protect them against solvent loss. This sensitivity also made it hard to obtain consistent TGA or magnetic measurements from the individual acetone solvate phases. After several attempts, consistent magnetic data were obtained from pure samples of $\mathbf{1}[\text{ClO}_4]_2\cdot \text{Me}_2\text{CO}$ and $\mathbf{1}[\text{ClO}_4]_2\cdot m\text{Me}_2\text{CO}\cdot 0.5\text{H}_2\text{O}$. However, the BF_4^- solvates could only be magnetically characterized as a mixture of the $\mathbf{1}[\text{BF}_4]_2\cdot \text{Me}_2\text{CO}$, $\mathbf{1}[\text{BF}_4]_2\cdot 0.75\text{Me}_2\text{CO}$ and $\mathbf{1}[\text{BF}_4]_2\cdot 0.5\text{Me}_2\text{CO}\cdot 0.5\text{H}_2\text{O}$ phases, which is labelled ' $\mathbf{1}[\text{BF}_4]_2\cdot x\text{Me}_2\text{CO}$ ' in the following discussion.

Mixed ' $\mathbf{1}[\text{BF}_4]_2\cdot x\text{Me}_2\text{CO}$ ' samples show $\chi_{\text{MT}} = 2.0 \pm 0.2 \text{ cm}^3 \text{ mol}^{-1} \text{ K}$ at 300 K, indicating a mixed high:low-spin population at room temperature. This stays roughly constant on cooling until 150 K when an abrupt decrease in χ_{MT} is observed, corresponding to an abrupt high \rightarrow low spin transition (Figure 1). A constant residual high-spin fraction with $\chi_{\text{MT}} = 0.5 \pm 0.2 \text{ cm}^3 \text{ mol}^{-1} \text{ K}$ remains on further cooling. The reverse low \rightarrow high spin-transition occurs at $T_{1/2} = 168 \pm 1$ K on rewarming. This is

always preceded by a small, gradual decrease in $\chi_M T$ between 100-150 K, which is characteristic for the thermal trapping of some SCO-active material in its high-spin form at such low temperatures.⁵¹⁻⁵⁵ That has also been seen in salts of other $[\text{Fe}(\text{bpp}^R)_2]^{2+}$ derivatives showing cooperative SCO at temperatures approaching 100 K.^{37,56-58}

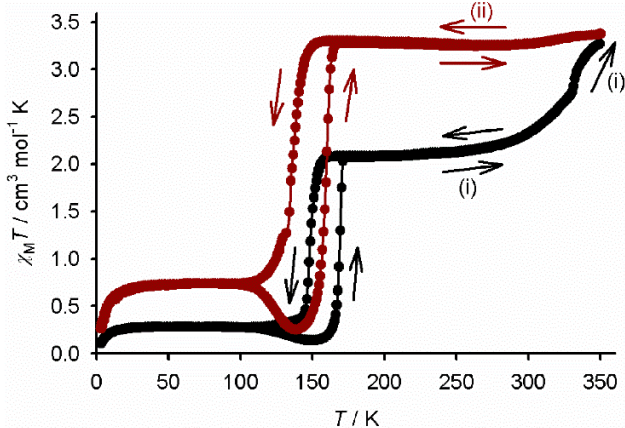


Figure 1. Magnetic susceptibility measurement for a mixed-phase sample of '1[BF₄]₂·xMe₂CO', showing its *in situ* conversion to 1[BF₄]₂·sf: (i) first cycle, 300→3→350 K (black); (ii) second cycle, 350→3→300 K (red). Data points are connected by spline curves for clarity. Scan rate 5 K min⁻¹.

While the temperature of the partial abrupt spin-transition in Figure 1 is consistent with single crystals of 1[BF₄]₂·Me₂CO (Figures S7-S8), the hysteresis loop is wider than expected from the unit cell data (Table 1).⁵⁰ That might be explained by the faster temperature ramp in the magnetic measurement, which can widen kinetic hysteresis in an SCO material.⁵⁹ Alternatively, it might reflect the onset of solvent loss from the sample in the high vacuum magnetometer cavity. In any case, the magnitude of the abrupt spin-transition implies samples of '1[BF₄]₂·xMe₂CO' contain between 35-55 % of cooperative SCO phase 1[BF₄]₂·Me₂CO.

Yellow 1[ClO₄]₂·Me₂CO is high-spin at room temperature and exhibits a complete, hysteretic spin transition centered at 162 K (Figure 2). As for the BF₄⁻ salt, the 22 K hysteresis width in the magnetic measurement is larger than in the single crystal. The discrepancy for this compound is only just outside the error of the crystallographic measurement, however (Table 1). In contrast, the brown material 1[ClO₄]₂·mMe₂CO·0.5H₂O exhibits gradual SCO with $T_{1/2} \approx 325$ K, which is *ca* 80 % complete at 350 K (Figure S24).

Heating '1[BF₄]₂·xMe₂CO' and 1[ClO₄]₂·Me₂CO to 350 K converts them to a new single-phase material, which was assigned as solvent-free 1X₂·sf from the single crystal experiments described below (Figures 1 and 2). The desolvation of '1[BF₄]₂·xMe₂CO' occurs rapidly in the magnetometer, within one thermal scan, but three or four scans were required for full conversion of 1[ClO₄]₂·Me₂CO to 1[ClO₄]₂·sf. Interestingly, all components of the '1[BF₄]₂·xMe₂CO' mixture transform to the same 1[BF₄]₂·sf material under these conditions. That was also observed for '1[ClO₄]₂·xMe₂CO' mixed phase samples (Figure S25).

The annealed 1X₂·sf samples are fully high-spin at room temperature and also exhibit abrupt spin-transitions below 200 K. The spin-transitions in both annealed materials also exhibit

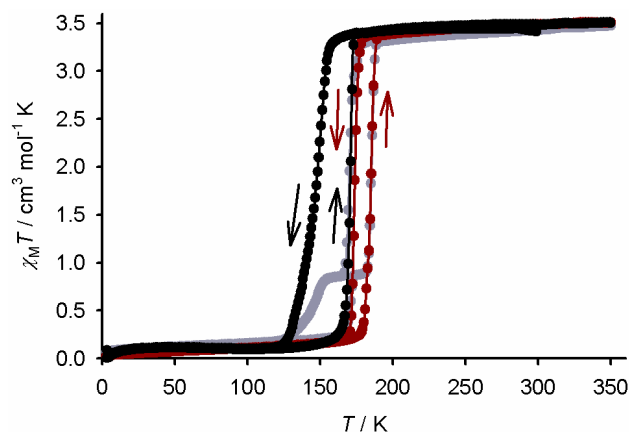


Figure 2. Magnetic susceptibility measurement for phase-pure 1[ClO₄]₂·Me₂CO, showing its *in situ* conversion to 1[ClO₄]₂·sf. Three consecutive thermal scans are shown: (i) 300→3→350 K (black); (ii) 350→3→350 K (gray); (iii) 350→3→300 K (red). Other details as for Figure 1.

thermal hysteresis. Interestingly, SCO in 1[BF₄]₂·sf occurs at *ca* 15 K lower temperature than for 1[BF₄]₂·Me₂CO, and with a wider thermal hysteresis (Figure 1). However, the opposite is observed for the perchlorate salt; $T_{1/2}$ for 1[ClO₄]₂·sf shifts to *ca* 10 K higher temperature, and with narrower hysteresis, after the desolvation process (Figure 2). A possible explanation for these differences is discussed below. Thermal trapping of a residual high-spin fraction of the sample was also observed during SCO in 1[BF₄]₂·sf, but not for 1[ClO₄]₂·sf. Thermal trapping in 1[BF₄]₂·sf occurs more efficiently when measured at a faster scan rate, confirming its kinetic origin (Figure S23).^{37,51-58}

Heating crystals of 1X₂·Me₂CO (X⁻ = BF₄⁻ or ClO₄⁻) at 370 K on the diffractometer caused a rapid transformation to 1X₂·sf (monoclinic, space group $P2_1/n$ $Z = 4$), without degradation of crystal quality. Unit cell determinations from 1X₂·sf confirmed their spin-transition temperatures match the magnetic data from the annealed '1X₂·xMe₂CO' samples (Figures 3 and S17-S19). However, the crystallographic SCO hysteresis loops for both 1X₂·sf crystals are a few degrees *wider* than in the magnetic data, which is the opposite to the trend expected if the hysteresis were controlled by the thermal scan rate (Table 1).⁵⁹ Rather, it might reflect the improved crystallinity and larger particle size of a single crystal of 1X₂·sf, compared to a polycrystalline sample from annealing a mixture of precursor phases.⁶⁰⁻⁶³

Structural comparison of 1X₂·Me₂CO and 1X₂·sf

The unit cells of 1X₂·sf (in the space group setting $P2_1/n$) resemble the precursor 1X₂·Me₂CO crystals (in the setting $P2_1/c$), but with the *b* and *c* axes exchanged; that is, $a \approx a'$, $b \approx c'$, $c \approx b'$ and $\beta \approx \beta'$. The cations in 1X₂·Me₂CO are roughly co-aligned, but with alternate canting of their molecular *z* axes about the crystallographic *c* direction (Figure 4). Cations related by a crystallographic inversion center exchange intermolecular $n \cdots \pi$ contacts through the β -S atom of each SS*i*Pr group. One of these $n \cdots \pi$ contacts is formed to a pyridyl ring from the neighbor molecule, while the other involves a pyrazolyl group. These pairwise $n \cdots \pi$ interactions propagate into chains parallel to the [101] crystal vector.

The chain-of- $n \cdots \pi$ -dimers motif is retained in 1X₂·sf. One dimerization interaction is geometrically similar in both lattice

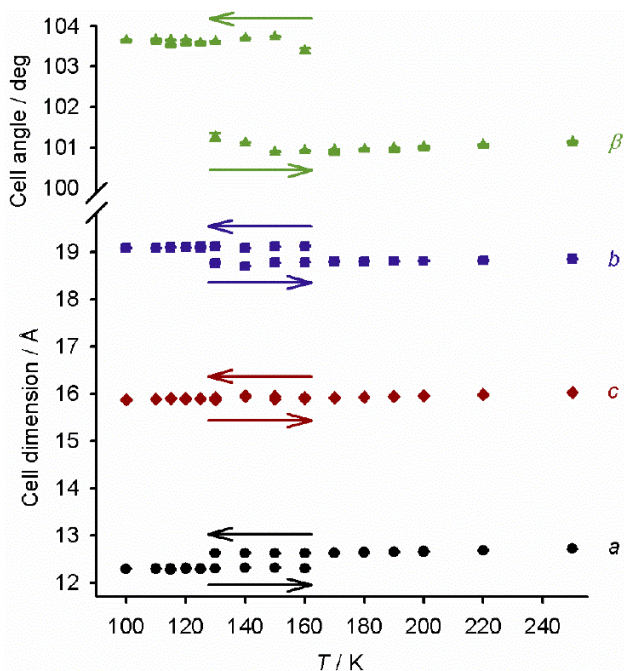


Figure 3. Variable temperature unit cell parameters for $1[\text{BF}_4]_2\cdot\text{sf}$, measured in cooling and warming modes and showing thermal hysteresis in the spin transition (Table S9).

types. However, each pair of cations in $1\text{X}_2\cdot\text{sf}$ is translated by $1+x, y, z$ compared to their equivalent positions in $1\text{X}_2\cdot\text{Me}_2\text{CO}$, so those S atoms interact with opposite faces of the heterocyclic ligand in the two lattice types. That gives the chains in $1\text{X}_2\cdot\text{sf}$ a zig-zag geometry, aligned along the $[010]$ vector (Figure 5).

The closest $\text{S}\cdots\pi$ distances for each interaction in the low-spin structures range from 3.26-3.44 Å for $1\text{X}_2\cdot\text{Me}_2\text{CO}$ and 3.31-3.50 Å for $1\text{X}_2\cdot\text{sf}$; these values are generally longer in the high-spin forms of the crystals (Tables S3 and S8). For comparison, the sum of the Pauling van der Waals radii of an S atom and an aromatic ring is 3.55 Å.⁶⁴ Hirshfeld surface analyses of these structures also highlight weak $\text{C}-\text{H}\cdots\text{Y}$ ($\text{Y} = \text{F}$ or O) and/or anion $\cdots\pi$ contacts between the cations and anions in some of the structures (Figures S35-S37).⁶⁵ These secondary interactions are less likely to contribute to SCO cooperativity however, since they do not directly link the cation switching centers in the materials.

Structures of both $1\text{X}_2\cdot\text{sf}$ crystals were determined at 250 K, when they were high-spin, and at 100 or 110 K. Both the low-spin and high-spin states of $1[\text{BF}_4]_2\cdot\text{sf}$ were achieved at 100 K, using the same crystal. That reflects the slow kinetics for that high \rightarrow low spin transition observed in the magnetic data (Figure 1). Thus, the crystal was thermally trapped in its high-spin form when it was first cooled from 250 to 100 K on the diffractometer,^{57,66-70} but a subsequent, duplicate experiment yielded the low-spin state at 100 K. The different outcomes might be

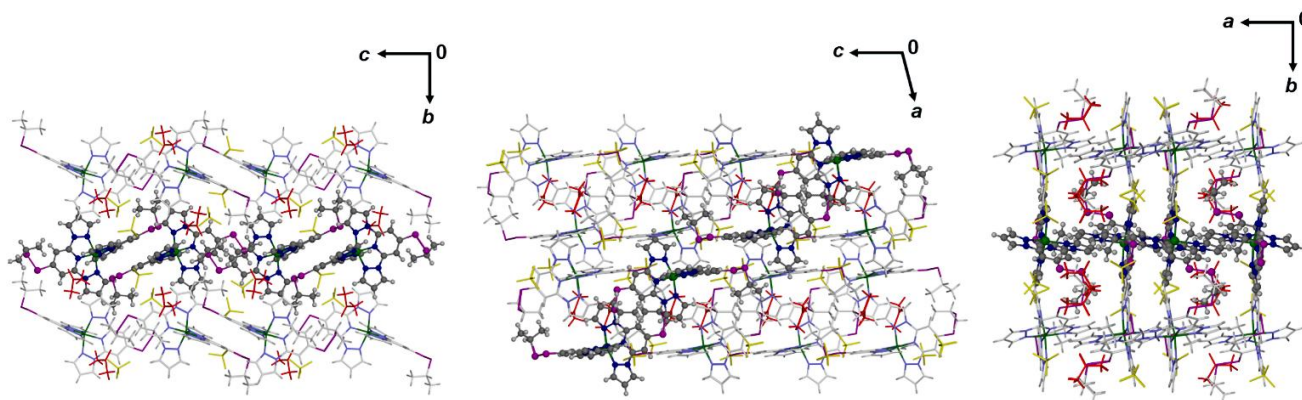


Figure 4. Packing diagrams of low-spin $1[\text{BF}_4]_2\cdot\text{Me}_2\text{CO}$ at 143 K, viewed along the $[100]$ (left), $[010]$ (center) and $[001]$ (right) crystal vectors. One chain of cations linked by $n\cdots\pi$ interactions is highlighted in each diagram, and the directions of the unit cell axes are shown for each view. Color code: C{complex}, white or dark gray; H{complex}, pale grey; N, pale or dark blue; S, purple; BF_4^- , yellow; solvent, red.

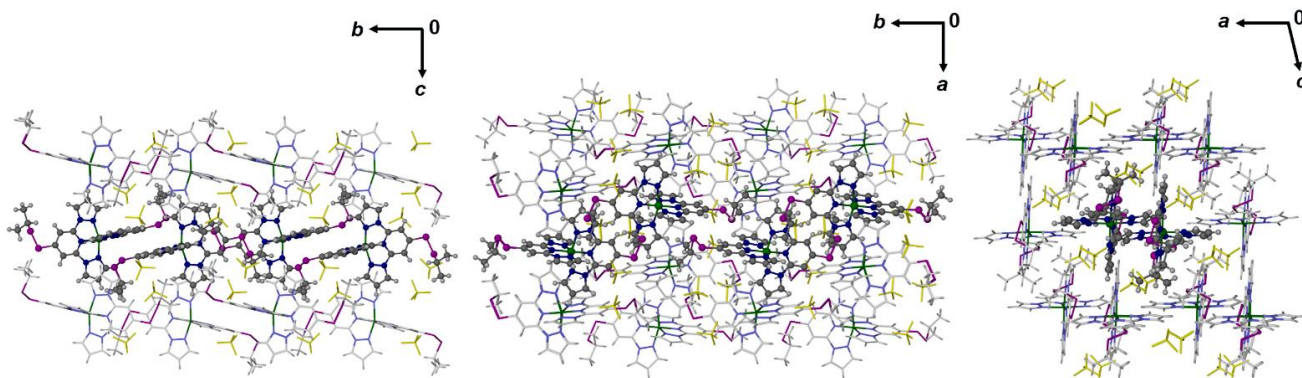


Figure 5. Packing diagrams of $1[\text{BF}_4]_2\cdot\text{sf}$ at 100 K, viewed along the $[100]$ (left), $[001]$ (center) and $[010]$ (right) crystal vectors. The views are arranged to facilitate comparison with the previous Figure. Details as for Figure 4.

Table 2. Crystallographic spin-transition temperatures for the $\mathbf{1X}_2\cdot\text{Me}_2\text{CO}$ and $\mathbf{1X}_2\cdot\text{sf}$ phases, and structural changes during their thermal SCO.^{a,b} The parameters are computed from high- and low-temperature crystal structures, with the values in square brackets for $\mathbf{1X}_2\cdot\text{sf}$ being calculated from their isothermal high-spin and low-spin structure refinements. More detailed metric parameters are listed in Tables S2 and S7.

| | $\mathbf{1}[\text{BF}_4]_2\cdot\text{Me}_2\text{CO}$ | $\mathbf{1}[\text{ClO}]_2\cdot\text{Me}_2\text{CO}$ | $\mathbf{1}[\text{BF}_4]_2\cdot\text{sf}$ | $\mathbf{1}[\text{ClO}]_2\cdot\text{sf}$ |
|------------------------|--|---|---|--|
| $T_{1/2\downarrow}$ | 175±5 ^c | 155±5 | 127.5±2.5 | 165±5 |
| $T_{1/2\uparrow}$ | 175±5 ^c | 165±5 | 165±5 | 185±5 |
| $\Delta T_{1/2}$ | – | 10±7 | 38±6 | 20±7 |
| ΔV_{Oh} | 2.419(15) | 2.439(14) | 2.555(17) [2.476(13)] | 2.548(15) [2.458(17)] |
| $\Delta\Sigma$ | 64.8(6) | 64.8(5) | 70.0(7) [69.2(6)] | 67.3(6) [63.1(6)] |
| $\Delta\Theta$ | 230 | 231 | 225 [216] | 218 [202] |
| $\Delta\phi$ | -11.32(16) | -11.47(15) | -11.99(19) [-13.03(16)] | -11.39(17) [-11.24(19)] |
| $\Delta\theta$ | -1.29(6) | -1.30(4) | -1.88(6) [-2.34(4)] | -1.06(5) [-1.15(5)] |

^a $\Delta V_{\text{Oh}} = V_{\text{Oh}}\{\text{high-spin}\} - V_{\text{Oh}}\{\text{low-spin}\}$. The other parameters in the table are calculated similarly. ^b V_{Oh} is the volume of the octahedron defined by the FeN_6 coordination sphere.⁷¹ Σ is a general measure of the deviation of a metal ion from an ideal octahedral geometry, while Θ more specifically indicates its distortion towards a trigonal prismatic structure.⁷¹⁻⁷³ ϕ is the *trans*-N{pyridyl}-Fe-N{pyridyl} bond angle, while θ is the dihedral angle between the least squares planes of the two tridentate ligands.⁷⁴ More detailed definitions and discussions of these parameters are in the cited references, and in the Supporting Information to this article. ^cSee ref. 50.

caused by small differences in the temperature ramp in the two experiments. Alternatively, they could reflect the introduction of additional defects or a reduction in domain size in the crystal following the first thermal cycle.⁶⁰⁻⁶³ While thermal trapping of $\mathbf{1}[\text{ClO}_4]_2\cdot\text{sf}$ was not observed, isothermal high- and low-spin structures of that compound were achieved at 170 K, a temperature inside its SCO hysteresis loop.

Although the orientations of their *i*Pr substituents are different, in other respects the molecular structures of $\mathbf{1X}_2\cdot\text{Me}_2\text{CO}$ and $\mathbf{1X}_2\cdot\text{sf}$ are very similar. Each shows a comparable displacement of one L^1 ligand relative to the other in the complex during SCO, as quantified by the *trans*-N{pyridyl}-Fe-N{pyridyl} bond angle (ϕ ; Table 2).⁷⁴ The four crystals show $163.01(13) \leq \phi \leq 166.37(12)^\circ$ when high-spin, which is a significant deviation from its ideal value of 180° . High-spin $[\text{Fe}(\text{bpp}^R)_2]^{2+}$ derivatives can show large distortions from idealized D_{2d} symmetry through reduced values of ϕ , and of the dihedral angle between the least squares planes of the two ligands (θ ; Table 2).²⁸ SCO in the solid state becomes more difficult as ϕ and θ deviate more strongly from the more regular geometries preferred by the low-spin complexes.²⁷ The values of ϕ in $\mathbf{1X}_2\cdot\text{Me}_2\text{CO}$ and for $\mathbf{1X}_2\cdot\text{sf}$ lie in a range where SCO is possible, but is rarely observed in practice.⁵⁷ The high-spin molecular geometries of $\mathbf{1X}_2\cdot\text{sf}$ appear to show a small temperature dependence, as we have observed before in some related compounds.^{19,75} More detailed investigations would be required to quantify that, however.

The low-spin forms of the compounds have more regular geometries with $174.33(10) \leq \phi \leq 177.61(13)^\circ$. The change in ϕ between the spin states, $\Delta\phi$, is 11-13° (Table 2), which leads to a large, anisotropic geometric rearrangement of the molecules in the lattice during SCO (Figure 6). Such $\Delta\phi$ values are unusually large for an SCO-active $[\text{Fe}(\text{bpp}^R)_2]^{2+}$ derivative, and are associated with cooperative hysteretic spin-transitions where they have been observed before.^{20,57,76,77} Notably $\mathbf{1}[\text{BF}_4]_2\cdot\text{sf}$, which shows a wider hysteresis loop than the other compounds in the Table, has both a larger $\Delta\phi$ and slightly higher $\Delta\theta$, which supports this structure: function relationship. These changes lead to lateral displacements of the peripheral atoms in the molecules, of up to 1.0 Å, which will be transmitted

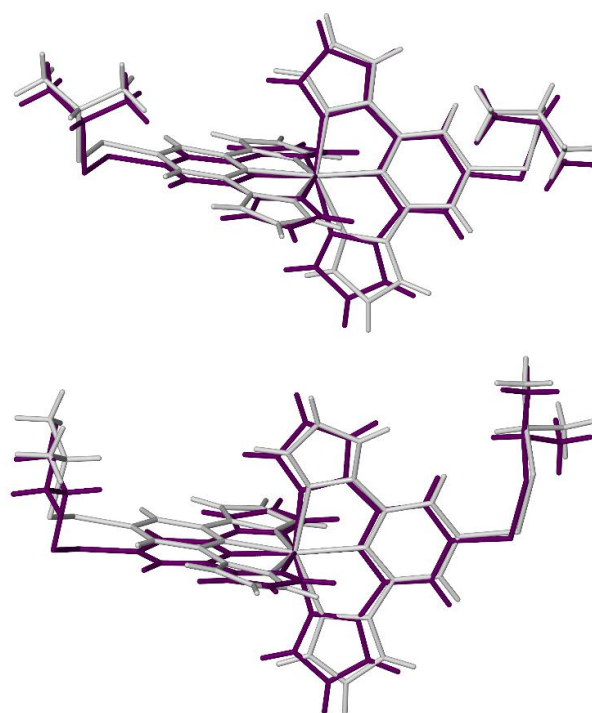


Figure 6. Overlaid high-spin (white) and low-spin (purple) structures of $\mathbf{1}[\text{BF}_4]_2\cdot\text{Me}_2\text{CO}$ (top) and $\mathbf{1}[\text{BF}_4]_2\cdot\text{sf}$ (bottom), showing the angular displacement of the L^1 ligands during SCO. Only the major orientation of the disordered *isopropyl* residue in high-spin $\mathbf{1}[\text{BF}_4]_2\cdot\text{Me}_2\text{CO}$ is shown. The $\mathbf{1}[\text{BF}_4]_2\cdot\text{sf}$ view was generated from the isothermal high- and low-spin structures of that compound at 100 K.

efficiently through the lattice by the intermolecular $n\cdots\pi$ interactions described above. This is the likely origin of the cooperative, hysteretic spin-transitions in $\mathbf{1X}_2\cdot\text{Me}_2\text{CO}$ and $\mathbf{1X}_2\cdot\text{sf}$.

Other $1\mathbf{X}_2$ ·solv materials

Recrystallization of the $1\mathbf{X}_2$ salts from undried nitromethane, acetonitrile or methanol yielded visually homogeneous samples of $1\mathbf{X}_2$ ·MeNO₂, $1\mathbf{X}_2$ ·MeCN and $1\mathbf{X}_2$ ·H₂O respectively. Crystals of $1[\mathbf{BF}_4]_2$ ·MeNO₂ and $1[\mathbf{ClO}_4]_2$ ·*n*MeNO₂ ($n \approx 0.9$; both monoclinic, $P2_1/n$, $Z = 4$) are isomorphous. The perchlorate crystal was slightly substoichiometric in nitromethane, which might reflect a steric clash between the solvent molecule and a neighboring, disordered ClO₄⁻ anion. Crystals of $1[\mathbf{BF}_4]_2$ ·H₂O (monoclinic, $P2_1/n$, $Z = 4$) are isomorphous with the nitromethane solvates and, although they were not crystallographically characterized, the X-ray powder patterns from $1[\mathbf{BF}_4]_2$ ·MeCN and $1[\mathbf{ClO}_4]_2$ ·H₂O imply they are also isomorphous with these materials (Figures S32-S33). However, $1[\mathbf{ClO}_4]_2$ ·MeCN (triclinic, $P\bar{1}$, $Z = 4$) adopts a different symmetry, with two unique cations in its asymmetric unit. All these materials are phase pure by powder diffraction except $1[\mathbf{ClO}_4]_2$ ·MeCN, whose powder pattern is different from the others and does not agree well with the crystallographic simulation. Although no other single crystal morphologies were apparent for that compound, bulk samples of $1[\mathbf{ClO}_4]_2$ ·MeCN appear to contain a mixture of phases.

The unit cell parameters of $1[\mathbf{BF}_4]_2$ ·MeNO₂, $1[\mathbf{BF}_4]_2$ ·H₂O and $1[\mathbf{ClO}_4]_2$ ·*n*MeNO₂ (in the space group setting $P2_1/n$) are also essentially identical to $1\mathbf{X}_2$ ·Me₂CO ($X^- = \mathbf{BF}_4^-$ or \mathbf{ClO}_4^- ; in the setting $P2_1/c$), with $a \approx a''$, $b \approx b''$, $c \approx c''$ and $\beta \approx \beta'$. However, despite that coincidental similarity, the crystal packing in the two solvate lattices is quite different. The cations in $1[\mathbf{BF}_4]_2$ ·MeNO₂, $1[\mathbf{BF}_4]_2$ ·H₂O and $1[\mathbf{ClO}_4]_2$ ·*n*MeNO₂ also associate into chains through intermolecular $n \cdots \pi$ interactions, involving sulfur atom lone pairs. However, pairs of interacting molecules in this lattice are related by a crystallographic C_2 axis, which associates them loosely into chains parallel to the [101] vector (Figure 7).

The intermolecular $S \cdots \pi$ distances in this lattice type range from 3.36-3.60 Å, and are a little longer than in the more cooperative $1\mathbf{X}_2$ ·Me₂CO and $1\mathbf{X}_2$ ·sf low-spin crystals (Table S13). While they are complicated by disorder, Hirshfeld surface analyses confirm there are no short, directional intermolecular interactions in these lattices (Figure S38).⁶⁵ Despite that, however, the overall packing density in this lattice type is greater than in the more cooperative materials, which is evidenced by the crystallographic density (D_c) of the compounds. For example, $1[\mathbf{ClO}_4]_2$ ·Me₂CO (M_r 947.69) has $D_c = 1.593 \text{ g cm}^{-3}$ at 100 K, while $1[\mathbf{ClO}_4]_2$ ·*n*MeNO₂ (M_r 944.55) gives $D_c = 1.614 \text{ g cm}^{-3}$ at the slightly higher temperature of 120 K.

The MeNO₂ and MeCN solvates are more stable to solvent loss than the acetone solvate crystals. These samples afforded TGA analyses consistent with their crystallographic formulations (Figure S31), and reproducible magnetic data. The hydrate crystals easily lose their lattice water on heating by TGA, but also regain it quickly when re-exposed to air. However those samples also gave reproducible magnetic data when protected against solvent loss.

All the MeNO₂, MeCN and H₂O solvates exhibit gradual SCO equilibria by magnetic susceptibility data, with $264 \leq T_{1/2} \leq 342 \text{ K}$ (Figures 8 and S34). Their high-temperature susceptibility behavior was reversible at temperatures up to 350 K, showing these spin-state changes are not associated with *in situ* solvent loss. The spin states shown by the magnetic data at different temperatures agree well with the crystallographic predictions, except for $1[\mathbf{ClO}_4]_2$ ·MeCN. The two unique cation environments in that crystal are both low-spin at 120 K and

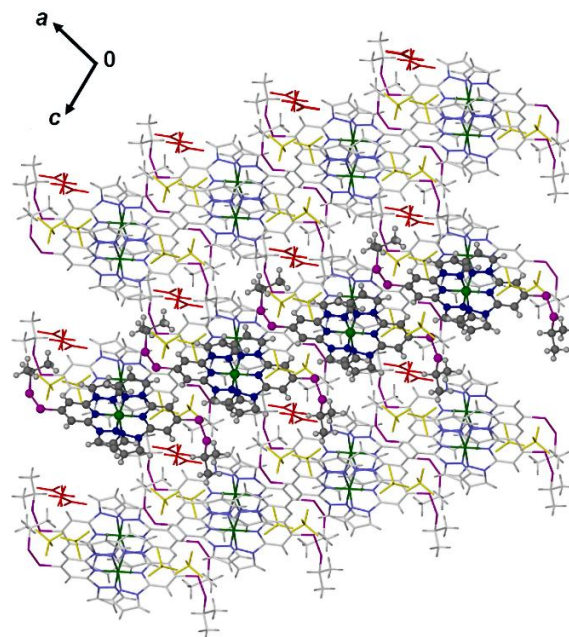


Figure 7. Packing diagram of $1[\mathbf{BF}_4]_2$ ·MeNO₂ at 120 K, viewed along the [010] vector. Only one orientation of the disordered residues in the structure is shown. One chain of cations linked by pairwise $n \cdots \pi$ interactions is highlighted, and the directions of the unit cell axes are shown. Color code: C{complex}, white or dark gray; H{complex}, pale grey; N, pale or dark blue; S, purple; \mathbf{BF}_4^- , yellow; solvent, red.

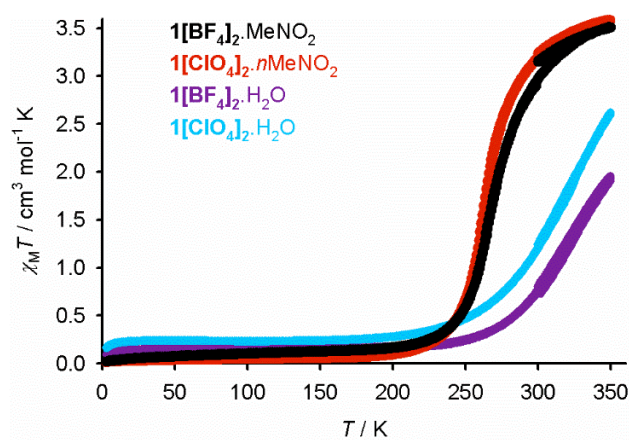


Figure 8. Variable temperature magnetic susceptibility data for the isomorphous $1\mathbf{X}_2$ ·MeNO₂ and $1\mathbf{X}_2$ ·H₂O materials. Data were measured on a 300→350→3→300 K thermal cycle, at a scan rate of 5 K min⁻¹.

predominantly high-spin at 250 K, implying they undergo SCO between those temperatures. However the bulk material undergoes gradual SCO at higher temperature, and is only 20 % high-spin at 250 K in the magnetic data. As mentioned above, this sample apparently contained a mixture of phases by powder diffraction, so the single crystal structures of $1[\mathbf{ClO}_4]_2$ ·MeCN are not representative of that bulk sample.

The isomorphous $1\mathbf{X}_2$ ·MeNO₂, $1\mathbf{X}_2$ ·MeCN or $1\mathbf{X}_2$ ·H₂O crystals could not be characterized in their high-spin form without crystal decomposition from solvent loss. Hence, it's unclear

whether their SCO is associated with smaller structural changes between their spin states, than in the more cooperative $\mathbf{1X}_2\text{Me}_2\text{CO}$ and $\mathbf{1X}_2\text{sf}$ series.⁷⁸

Annealing crystals of $\mathbf{1}[\text{BF}_4]_2\text{MeNO}_2$ and $\mathbf{1}[\text{BF}_4]_2\text{H}_2\text{O}$ at 370 K for 1 hr on the diffractometer afforded the same $\mathbf{1}[\text{BF}_4]_2\text{sf}$ phase described above. These annealed crystals were often twinned, but retained their single crystallinity on some occasions. The transformation is not evident in the magnetic data from the same phases however, implying it requires more forcing conditions than for the acetone solvates (Figure 8).

Spin-crossover in $\mathbf{2}[\text{BF}_4]_2$

Since L^2 was available in small quantities, only one salt of its iron complex was investigated, $\mathbf{2}[\text{BF}_4]_2$. Two isomorphous solvates of this material were structurally characterized, $\mathbf{2}[\text{BF}_4]_2\cdot 0.5\text{MeNO}_2$ and $\mathbf{2}[\text{BF}_4]_2\cdot 0.5\text{MeCN}$ (both triclinic, $P\bar{1}$, $Z = 2$). These were low-spin at 100 and 120 K, respectively, while a second structure determination of $\mathbf{2}[\text{BF}_4]_2\cdot 0.5\text{MeNO}_2$ confirmed it remains low-spin at room temperature (Figures S40-S41, Table S14). A third measurement at 350 K led to twinning of the crystal however, which we were unable to resolve.

Variable temperature magnetic data from $\mathbf{2}[\text{BF}_4]_2\cdot 0.5\text{MeNO}_2$ proved unexpectedly complicated (Figure 9). The freshly prepared compound is low-spin at 290 K, as expected, but transforms abruptly just above room temperature to a predominantly high-spin material ($\chi_M T = 2.8 \text{ cm}^3 \text{ mol}^{-1} \text{ K}$ at 340 K). A further small increase in $\chi_M T$ between 340-350 K implies its SCO continues in more gradual fashion on further heating. The high→low-spin SCO upon recooling occurs gradually and in three apparent steps near 340, 275 and 200 K; the material only regains its fully low-spin state below 140 K. The 200 K feature, which is starred in Figure 9, appears in both heating and cooling modes in scans (ii)-(iv) and slowly grows in each successive scan. The other features of the susceptibility curve are reproducible in all four scans, however.

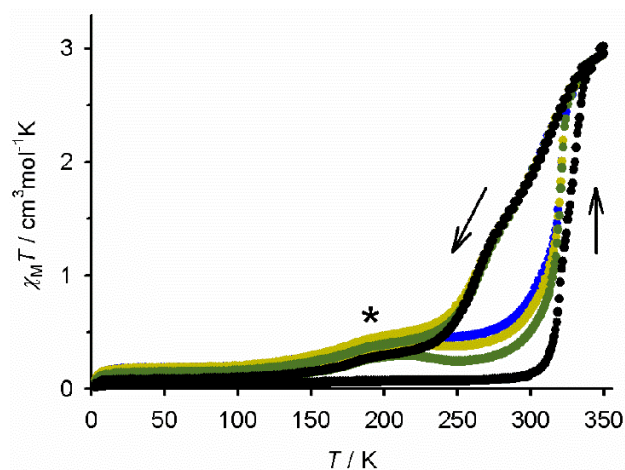


Figure 9. Variable temperature magnetic susceptibility data for $\mathbf{2}[\text{BF}_4]_2\cdot 0.5\text{MeNO}_2$. Four consecutive thermal scans are shown (Figure S43): (i) 300→3→350→3 K (black); (ii) 3→350→3 K (green); (iii) 3→350→3 K (yellow); (iv) 3→350→300 K (blue). Scan rate 5 K min⁻¹. The starred feature grows on repeated scanning, and may arise from slow desolvation of the sample as the experiment proceeds.

The structural origin of this unusual behavior could not be probed in detail, because crystal structures of $[\text{BF}_4]_2\cdot 0.5\text{MeNO}_2$ following the low→high-spin transformation are unavailable. However, we postulate an abrupt crystallographic phase change from a low-spin-phase phase A to an SCO-active phase B, on heating above 300 K. Phase B would then undergo gradual SCO on cooling, in two steps around 340 and 275 K, and transform back to phase A at lower temperature after regaining its low-spin state. Phase B may contain two or more unique iron environments in its crystal lattice, to account for the stepwise SCO in cooling mode.⁷⁹⁻⁸³ Superimposed on this reversible behavior, the starred feature near 200 K may arise from partial desolvation of the sample on heating, which becomes more pronounced as the experiment proceeds. TGA data show minimal solvent loss from the material below 340 K, which is consistent with that suggestion (Figure S44).

Conclusion

This study reports solvate compounds of $[\text{Fe}(L^1)_2]\text{X}_2$ ($\mathbf{1X}_2$; $\text{X}^- = \text{BF}_4^-$ or ClO_4^-). Many of the materials adopt one of three lattice types ($\mathbf{1X}_2\text{Me}_2\text{CO}$, $\mathbf{1X}_2\text{sf}$ and $\mathbf{1X}_2\text{MeNO}_2/\mathbf{1X}_2\text{H}_2\text{O}$) exhibiting similar unit cell dimensions, but in different monoclinic space group settings. These adopt different packing motifs based on chains of $[\text{Fe}(L^1)_2]^{2+}$ molecules linked by pairwise, intermolecular $n\cdots\pi$ interactions involving their disulfanyl $\beta\text{-S}$ atoms (Figures S6, S16 and S30). The relationship between these structures is emphasized by the fact that $\mathbf{1X}_2\text{sf}$ is prepared from $\mathbf{1X}_2\text{Me}_2\text{CO}$ in single-crystal-to-single-crystal fashion; the transformation is so facile that it makes $\mathbf{1X}_2\text{Me}_2\text{CO}$ difficult to characterize. Some $\mathbf{1X}_2\text{MeNO}_2/\mathbf{1X}_2\text{H}_2\text{O}$ crystals were also converted to $\mathbf{1X}_2\text{sf}$ after more extended annealing on the diffractometer.

While not all the intermolecular $n\cdots\pi$ contacts are notably short, they afford a large surface contact area between nearest neighbor cations that could facilitate cooperative SCO switching. Thus, both $\mathbf{1X}_2\text{Me}_2\text{CO}$ and $\mathbf{1X}_2\text{sf}$ exhibit abrupt thermal spin-transitions at $T_{1/2} = 150 \pm 20 \text{ K}$, with thermal hysteresis widths of up to 38 K depending on the measurement method (Figures 1-3). However the hysteresis widths for these compounds determined by crystallographic and magnetic measurement do not follow a consistent trend (Table 1), which implies solid state kinetics⁵⁹ and sample crystallinity⁶⁰⁻⁶³ may both contribute to the form of the transitions. All four crystals undergo a rearrangement of molecular structure between their spin states, involving a large angular displacement of their L^1 ligands (Table 2). This angular rearrangement is somewhat greater for $\mathbf{1}[\text{BF}_4]_2\text{sf}$, whose SCO hysteresis loop is also wider than for the other crystals.

This observation can explain the wider anion dependence of the effect of single-crystal-to-single-crystal desolvation of $\mathbf{1X}_2\text{Me}_2\text{CO}$ on their SCO properties. The molecular structures of the two spin states in $\mathbf{1}[\text{ClO}_4]_2\text{Me}_2\text{CO}$ and $\mathbf{1}[\text{ClO}_4]_2\text{sf}$ are very similar. However, $\mathbf{1}[\text{BF}_4]_2\text{sf}$ undergoes a greater structural rearrangement during SCO compared to $\mathbf{1}[\text{BF}_4]_2\text{Me}_2\text{CO}$. That larger structural change should increase the activation energy of SCO in $\mathbf{1}[\text{BF}_4]_2\text{sf}$, widening its hysteresis loop. Moreover, the more distorted molecular structure in the high-spin $\mathbf{1}[\text{BF}_4]_2\text{sf}$ crystal will destabilize its low-spin state, thus lowering $T_{1/2}$ as observed.²⁷

Compounds adopting the third variant of this packing structure, $\text{IX}_2\cdot\text{MeNO}_2/\text{IX}_2\cdot\text{H}_2\text{O}$, exhibit more typically gradual thermal SCO equilibria centered at higher temperatures. While no high-spin crystal structures were achieved, that may imply the structure changes during SCO are smaller for this series. Notably, the less cooperative $\text{IX}_2\cdot\text{MeNO}_2/\text{IX}_2\cdot\text{H}_2\text{O}$ lattice also has a higher crystal packing density than more cooperative $\text{IX}_2\cdot\text{Me}_2\text{CO}$. One might expect a denser crystal to exhibit more cooperative switching behavior, other things being equal, but that is not the case in this system. In fact, the literature contains examples of polymorphic or closely related SCO materials where a higher crystal density is associated with both stronger^{84,85} or weaker^{86–88} transition cooperativity.

Lastly, $2[\text{BF}_4]_2\cdot 0.5\text{MeNO}_2$ undergoes abrupt SCO with an unusual asymmetric hysteresis loop, which is centered around room temperature and has at least two steps in its more gradual cooling branch (Figure 9). We know of one other material whose spin-transition profile resembles Figure 9, but without steps on the cooling branch of the transition.⁸⁹ Some other compounds exhibit spin-transitions with more abrupt, unsymmetric, stepped hysteresis loops.^{17,35,90–95} Where structural data are available, the asymmetry always reflects a crystallographic phase change during SCO, as proposed here.^{35,89–92} The high-spin and low-spin phases then have different lattice structures, which can lead to different transition cooperativity in the low→high-spin and high→low-spin processes. The forward and reverse crystallographic phase changes can also occur at different rates, especially where thermal hysteresis dictates they take place at very different temperatures.^{96,97}

This work has afforded structure: function correlations for SCO in IX_2 solvate salts, in three related crystal lattices. The structure types exhibit similar unit cell dimensions, and variations of a crystal packing motif based on chains of cations linked by pairwise intermolecular $\text{S}\cdots\pi$ contacts. Their structural similarity makes them especially valuable for determining the structural basis of cooperative phase transitions in SCO compounds, and other types of functional molecular crystal.

ASSOCIATED CONTENT

Supporting Information.

Synthetic details and characterization data for the new ligand L^1 ; experimental data, refinement procedures and tabulated metric parameters for the crystal structure determinations; Hirshfeld fingerprint maps; X-ray powder diffraction and TGA data; and, additional solid state and solution magnetic susceptibility measurements (PDF).

Accession Codes

CCDC 2123746–2123772 contain the supplementary crystallographic data for this paper. These data can be obtained free of charge via www.ccdc.cam.ac.uk/data_request/cif, or by emailing data_request@ccdc.cam.ac.uk, or by contacting The Cambridge Crystallographic Data Center, 12 Union Road, Cambridge CB2 1EZ, UK; fax: +44 1223 336033.

Data Sets

Experimental data sets associated with this paper are available from the University of Leeds library (<http://doi.org/10.5518/1098>).

AUTHOR INFORMATION

Corresponding Author

*Email address for MAH: m.a.halcrow@leeds.ac.uk.

Present Address

¶ Department of Chemistry, University of Liverpool, Crown Street, Liverpool, L69 7ZD, UK.

Author Contributions

All authors have given approval to the final version of the manuscript.

Notes

The authors declare no competing financial interests.

ACKNOWLEDGMENT

The authors thank Simon Barrett (University of Leeds) for the solution magnetic measurements in the Supporting Information. This work was funded by the EPSRC (EP/I014039/1 and EP/K012576/1).

REFERENCES

- (1) Gütllich, P.; Goodwin, H. A. (eds.) *Spin Crossover in Transition Metal Compounds I–III, Topics in Current Chemistry*; Springer-Verlag: Berlin, 2004; Vols. 233–235.
- (2) Halcrow, M. A. (ed), *Spin-Crossover Materials - Properties and Applications*, John Wiley & Sons, Ltd.: New York, 2013, p. 568.
- (3) Zarembowitch, J.; Varret, F.; Hauser, A.; Real, J. A.; Boukheddaden, K. Spin Crossover Phenomenon – Preface and Introduction. *C. R. Chimie* **2018**, *21*, 1056–1059.
- (4) Kumar, K. S.; Ruben, M. Emerging Trends in Spin Crossover (SCO) Based Functional Materials and Devices. *Coord. Chem. Rev.* **2017**, *346*, 176–205.
- (5) Molnár, G.; Rat, S.; Salmon, L.; Nicolozzi, W.; Bousseksou, A. Spin Crossover Nanomaterials: From Fundamental Concepts to Devices. *Adv. Mater.* **2018**, *30*, 1703862.
- (6) Yao, Z.-S.; Tang, Z.; Tao, J. Bistable Molecular Materials with Dynamic Structures. *Chem. Commun.* **2020**, *56*, 2071–2086.
- (7) Huang, W.; Ma, X.; Sato, O.; Wu, D. Controlling Dynamic Magnetic Properties of Coordination Clusters via Switchable Electronic Configuration. *Chem. Soc. Rev.* **2021**, *50*, 6832–6870.
- (8) Guionneau, P.; Marchivie, M.; Chastanet, G. Multiscale Approach of Spin Crossover Materials: a Concept Mixing Russian Dolls and Domino Effects. *Chem. – Eur. J.* **2021**, *27*, 1483–1486.
- (9) Halcrow, M. A. Structure:Function Relationships in Molecular Spin-Crossover Complexes. *Chem. Soc. Rev.* **2011**, *40*, 4119–4142.
- (10) Guionneau, P.; Létard, J.-F.; Yufit, D. S.; Chasseau, D.; Bravic, G.; Goeta, A. E.; Howard, J. A. K.; Kahn, O. Structural Approach of the Features of the Spin Crossover Transition in Iron(II) Compounds. *J. Mater. Chem.* **1999**, *9*, 985–994.
- (11) Hostettler, M.; Törnroos, K. W.; Chernyshov, S.; Vangdal, B.; Bürgi, H.-B. Challenges in Engineering Spin Crossover: Structures and Magnetic Properties of Six Alcohol Solvates of Iron(II) Tris(2-picolylamine) Dichloride. *Angew. Chem. Int. Ed.* **2004**, *43*, 4589–4594.
- (12) Yamada, M.; Hagiwara, H.; Torigoe, H.; Matsumoto, N.; Kojima, M.; Dahan, F.; Tuchagues, J.-P.; Re, N.; Iijima, S. A Variety of Spin-Crossover Behaviors Depending on the Counter Anion: Two-Dimensional Complexes Constructed by $\text{NH}\cdots\text{Cl}^-$ Hydrogen Bonds, $[\text{Fe}^{\text{II}}\text{H}_3\text{L}^{\text{Me}}]\text{Cl}\cdot\text{X}$ ($\text{X} = \text{PF}_6^-, \text{AsF}_6^-, \text{SbF}_6^-, \text{CF}_3\text{SO}_3^-$; $\text{H}_3\text{L}^{\text{Me}} = \text{Tris}[\{2-[(2\text{-methylimidazol-4-yl)methylidene]amino\}ethyl]amine$). *Chem. – Eur. J.* **2006**, *12*, 4536–4549.
- (13) Sato, T.; Nishi, K.; Iijima, S.; Kojima, M.; Matsumoto, N. One-Step and Two-Step Spin-Crossover Iron(II) Complexes of ((2-Methylimidazol-4-yl)methylidene)histamine, *Inorg. Chem.* **2009**, *48*, 7211–7229.
- (14) Pritchard, R.; Kilner, C. A.; Halcrow, M. A. Iron(II) Complexes With a Terpyridine Embrace Packing Motif Show Remarkably Consistent Cooperative Spin-Transitions. *Chem. Commun.* **2007**, *2007*, 577–579.
- (15) Wei, R.-J.; Tao, J.; Huang, R.-B.; Zheng, L.-S. Reversible and Irreversible Vapor-Induced Guest Molecule Exchange in Spin-Crossover Compounds. *Inorg. Chem.* **2011**, *50*, 8553–8564.

- (16) Sun, X.-P.; Wei, R.-J.; Yao, Z.-S.; Tao, J. Solvent Effects on the Structural Packing and Spin-Crossover Properties of a Mononuclear Iron(II) Complex. *Cryst. Growth Des.* **2018**, *18*, 6853–6862.
- (17) Phonsri, W.; Harding, P.; Liu, L.; Telfer, S. G.; Murray, K. S.; Moubaraki, B.; Ross, T. M.; Jameson, G. N. L.; Harding, D. J. Solvent Modified Spin Crossover in an Iron(III) Complex: Phase Changes and an Exceptionally Wide Hysteresis. *Chem. Sci.* **2017**, *8*, 3949–3959.
- (18) Díaz-Torres, R.; Phonsri, W.; Murray, K. S.; Liu, L.; Ahmed, M.; Neville, S. M.; Harding, P.; Harding, D. J. Spin Crossover in Iron(III) Quinolyalsalicylaldiminates: the Curious Case of $[\text{Fe}(\text{qsal-F})_2](\text{Anion})$. *Inorg. Chem.* **2020**, *59*, 13784–13791.
- (19) Kulmaczewski, R.; Trzop, E.; Collet, E.; Vela, S.; Halcrow, M. A. Structure:Function Relationships for Thermal and Light-Induced Spin-Crossover in Isomorphous Molecular Materials. *J. Mater. Chem. C* **2020**, *8*, 8420–8429.
- (20) Capel Berdiell, I.; Kulmaczewski, R.; Shahid, N.; Cespedes, O.; Halcrow, M. A. The Number and Shape of Lattice Solvent Molecules Controls Spin-Crossover in an Isomorphous Series of Crystalline Solvate Salts. *Chem. Commun.* **2021**, *57*, 6566–6569.
- (21) Shatruk, M.; Phan, H.; Chrisostomo, B. A.; Suleimenova, A. Symmetry-Breaking Structural Phase Transitions in Spin Crossover Complexes. *Coord. Chem. Rev.* **2015**, *289–290*, 62–73.
- (22) Ortega-Villar, N.; Muñoz, M. C.; Real, J. A. Symmetry Breaking in Iron(II) Spin-Crossover Molecular Crystals. *Magnetochemistry* **2016**, *2*, 16.
- (23) Dorbes, S.; Valade, L.; Real, J. A.; Faulmann, C. $[\text{Fe}(\text{sal-trien})][\text{Ni}(\text{dmit})_2]$: Towards Switchable Spin Crossover Molecular Conductors. *Chem. Commun.* **2005**, *2005*, 69–71.
- (24) Craig, G. A.; Costa, J. S.; Roubeau, O.; Teat, S. J.; Aromí, G. Coupled Crystallographic Order–Disorder and Spin State in a Bistable Molecule: Multiple Transition Dynamics. *Chem. – Eur. J.* **2011**, *17*, 3120–3127.
- (25) Shao, D.; Shi, L.; Shen F.-X.; Wei, X.-Q.; Sato, O.; Wang, X.-Y. Reversible On–Off Switching of the Hysteretic Spin Crossover in a Cobalt(II) Complex via Crystal to Crystal Transformation. *Inorg. Chem.* **2019**, *58*, 11589–11598.
- (26) Shepherd, H. J.; Palamarcic, T.; Rosa, P.; Guionneau, P.; Molnár, G.; Létard, J.-F.; Bousseksou, A. Antagonism between Extreme Negative Linear Compression and Spin Crossover in $[\text{Fe}(\text{dpp})_2(\text{NCS})_2] \cdot \text{py}$. *Angew. Chem. Int. Ed.* **2012**, *51*, 3910–3914.
- (27) Halcrow, M. A. Iron(II) Complexes of 2,6-Di(pyrazol-1-yl)pyridines – a Versatile System for Spin-Crossover Research. *Coord. Chem. Rev.* **2009**, *253*, 2493–2514.
- (28) Kershaw Cook, L. J.; Mohammed, R.; Sherborne, G.; Roberts, T. D.; Alvarez, S.; Halcrow, M. A. Spin State Behaviour of Iron(II)/Dipyrazolopyridine Complexes. New Insights from Crystallographic and Solution Measurements. *Coord. Chem. Rev.* **2015**, *289–290*, 2–12.
- (29) Vela, S.; Novoa, J. J.; Ribas-Arino, J. Insights into the Crystal-Packing Effects on the Spin Crossover of $[\text{Fe}^{\text{II}}(\text{1-bpp})_2]^{2+}$ -Based Materials. *Phys. Chem. Chem. Phys.* **2014**, *16*, 27012–27024.
- (30) Olguín, J.; Brooker, S. Spin Crossover Active Iron(II) Complexes of Selected Pyrazole-Pyridine/Pyrazine Ligands. *Coord. Chem. Rev.* **2011**, *255*, 203–240.
- (31) Attwood, M.; Turner, S. S. Back to Back 2,6-Bis(Pyrazol-1-yl)pyridine and 2,2':6',2''-Terpyridine Ligands: Untapped Potential for Spin Crossover Research and Beyond. *Coord. Chem. Rev.* **2017**, *353*, 247–277.
- (32) Kershaw Cook, L. J.; Kulmaczewski, R.; Mohammed, R.; Dudley, S.; Barrett, S. A.; Little, M. A.; Deeth, R. J.; Halcrow, M. A. A Unified Treatment of the Relationship Between Ligand Substituents and Spin State in a Family of Iron(II) Complexes. *Angew. Chem. Int. Ed.* **2016**, *55*, 4327–4331.
- (33) Halcrow, M. A.; Capel Berdiell, I.; Pask, C. M.; Kulmaczewski, R. The Relationship Between Molecular Structure and Switching Temperature in a Library of Spin-Crossover Molecular Materials. *Inorg. Chem.* **2019**, *58*, 9811–9821.
- (34) Kershaw Cook, L. J.; Shepherd, H. J.; Comyn, T. P.; Baldé, C.; Cespedes, O.; Chastanet, G.; Halcrow, M. A. Decoupled Spin-Crossover and Structural Phase Transition in a Molecular Iron(II) Complex. *Chem. – Eur. J.* **2015**, *21*, 4805–4816.
- (35) Kershaw Cook, L. J.; Kulmaczewski, R.; Barrett, S. A.; Halcrow, M. A. Iron(II) Complexes of 4-Sulfanyl-, 4-Sulfinyl- and 4-Sulfonyl-2,6-Dipyrazolopyridine Ligands. A Subtle Interplay Between Spin-Crossover and Crystallographic Phase Changes. *Inorg. Chem. Front.* **2015**, *2*, 662–670.
- (36) Kershaw Cook, L. J.; Kulmaczewski, R.; Cespedes, O.; Halcrow, M. A. Different Spin State Behaviors in Isostructural Solvates of a Molecular Iron(II) Complex. *Chem. – Eur. J.* **2016**, *22*, 1789–1799.
- (37) Kulmaczewski, R.; Trzop, E.; Kershaw Cook, L. J.; Collet, E.; Chastanet, G.; Halcrow, M. A. Role of Symmetry Breaking in the Structural Trapping of Light-Induced Excited Spin States. *Chem. Commun.* **2017**, *53*, 13268–13271.
- (38) Kulmaczewski, R.; Bamiduro, F.; Cespedes, O.; Halcrow, M. A. Structural Transformations and Spin-Crossover in $[\text{FeL}_2]^{2+}$ Salts ($L = 4\text{-}\{Terbutylsulfanyl\}\text{-}2,6\text{-di}\{\text{pyrazol-1-yl}\}\text{pyridine}$) – the Influence of Bulky Ligand Substituents. *Chem. – Eur. J.* **2021**, *27*, 2082–2092.
- (39) Since this work was done, we've found it more convenient to prepare bpp^{SR} derivatives in one pot, by treating 2,4,6-trifluoropyridine sequentially with 1 equiv sodium alkylthiolate, then 2 equiv sodium pyrazolate.^{38,98} As for our original method (Scheme S1), the product mixture from the new reaction requires an extended purification. However, this is quicker than using bpp^{SH} as a starting material, which itself requires 3 steps to prepare.⁴⁹ This new synthesis of bpp^{SR} ligands does not afford bpp^{SSR} byproducts like L^1 or L^2 , however.
- (40) Xue, S.; Guo, Y.; Garcia, Y. Spin Crossover Crystalline Materials Engineered via Single-Crystal-to-Single-Crystal Transformations. *CrystEngComm* **2021**, *23*, 7899–7915.
- (41) Fernandez-Bartolome, E.; Martinez-Martinez, A.; Resines-Urien, E.; Piñeiro-Lopez, L.; Costa, J. S. Reversible Single-Crystal-to-Single-Crystal Transformations in Coordination Compounds Induced by External Stimuli. *Coord. Chem. Rev.* **2022**, *452*, 214281.
- (42) Sheldrick, G. M. Crystal Structure Refinement with *SHELXL*. *Acta Cryst. Sect. C: Struct. Chem.* **2015**, *71*, 3–8.
- (43) Barbour, L. J. *X-Seed 4*: Updates to a Program for Small-Molecule Supramolecular Crystallography. *J. Appl. Cryst.* **2020**, *53*, 1141–1146.
- (44) Dolomanov, O. V.; Bourhis, L. J.; Gildea, R. J.; Howard, J. A. K.; Puschmann, H. *OLEX2*: a Complete Structure Solution, Refinement and Analysis Program. *J. Appl. Cryst.* **2009**, *42*, 339–341.
- (45) Turner, M. J.; McKinnon, J. J.; Wolff, S. K.; Grimwood, D. J.; Spackman, P. R.; Jayatilaka, D.; Spackman, M. A. *CrystalExplorer17*, University of Western Australia, 2017, <http://hirshfeldsurface.net>.
- (46) O'Connor, C. J. Magnetochemistry – Advances in Theory and Experimentation. *Prog. Inorg. Chem.* **1982**, *29*, 203–283.
- (47) Schubert, E. M. Utilizing the Evans Method with a Superconducting NMR Spectrometer in the Undergraduate Laboratory. *J. Chem. Educ.* **1992**, *69*, 62.
- (48) García, B.; Ortega, J. C. Excess Viscosity η^E , Excess Volume V^E , and Excess Free Energy of Activation ΔG^{*E} at 283, 293, 303, 313, and 323 K for Mixtures of Acetonitrile and Alkyl Benzoates. *J. Chem. Eng. Data* **1988**, *33*, 200–204.
- (49) Kershaw Cook, L. J.; Fisher, J.; Harding, L. P.; Halcrow, M. A. An Iron(II) Spin-Crossover Metallacycle from a Back-To-Back Bis[dipyrazolopyridine]. *Dalton Trans.* **2015**, *44*, 9417–9425.
- (50) Unit cells were measured at 10 K temperature intervals. The forward and reverse spin-transitions in $1[\text{BF}_4]_2 \cdot \text{Me}_2\text{CO}$ both occurred between 170 and 180 K, so its spin transition could exhibit thermal hysteresis of up to ca 10 K (as found for $1[\text{ClO}_4]_2 \cdot \text{Me}_2\text{CO}$), while falling outside the resolution of the measurement.
- (51) Ritter, G.; König, E.; Irlér, W.; Goodwin, H. A. The High-Spin (6T_2) \rightleftharpoons Low-Spin (1A_1) Transition in Solid Bis[2-(2-pyridylamino)-4-(2-pyridyl)thiazole]iron(II) Dinitrate. Its Dependence on Time and on the Previous History of the Specimen. *Inorg. Chem.* **1978**, *17*, 224–228.
- (52) Létard, J.-F.; Asthana, S.; Shepherd, H. J.; Guionneau, P.; Goeta, A. E.; Suemura, N.; Ishikawa, R.; Kaizaki, S. Photomagnetism of a *sym-cis*-Dithiocyanato Iron(II) Complex with a Tetradentate *N,N'*-Bis(2-pyridylmethyl)1,2-ethanediamine Ligand. *Chem. – Eur. J.* **2012**, *18*, 5924–5934.
- (53) Paradis, N.; Chastanet, G.; Létard, J.-F. When Stable and Metastable HS States Meet in Spin-Crossover Compounds. *Eur. J. Inorg. Chem.* **2012**, *2012*, 3618–3624.

- (54) Paradis, N.; Chastanet, G.; Palamarcic, T.; Rosa, P.; Varret, F.; Boukheddaden, K.; Létard, J.-F. Detailed Investigation of the Interplay Between the Thermal Decay of the Low Temperature Metastable HS State and the Thermal Hysteresis of Spin-Crossover Solids. *J. Phys. Chem. C* **2015**, *119*, 20039–20050.
- (55) Ye, Y. S.; Chen, X. Q.; Cai, Y. D.; Fei, B.; Dechambenoit, P.; Rouzières, M.; Mathonière, C.; Clérac, R.; Bao, X. Slow Dynamics of the Spin-Crossover Process in an Apparent High-Spin Mononuclear Fe^{II} Complex. *Angew. Chem. Int. Ed.* **2019**, *58*, 18888–18891.
- (56) Money, V. A.; Carbonera, C.; Elhaik, J.; Halcrow, M. A.; Howard, J. A. K.; Létard, J.-F. Interplay Between Kinetically Slow Thermal Spin-Crossover and Metastable High-Spin State Relaxation in an Iron(II) Complex with Similar $T_{1/2}$ and $T(\text{LIESST})$. *Chem. – Eur. J.* **2007**, *13*, 5503–5514.
- (57) Kershaw Cook, L. J.; Thorp-Greenwood, F. L.; Comyn, T. P.; Cespedes, O.; Chastanet, G.; Halcrow, M. A. Unexpected Spin-Crossover and a Low Pressure Phase Change in an Iron(II)/Dipyrazolylpyridine Complex Exhibiting a High-Spin Jahn-Teller Distortion. *Inorg. Chem.* **2015**, *54*, 6319–6330.
- (58) Galadzhun, I.; Kulmaczewski, R.; Shahid, N.; Cespedes, O.; Howard, M. J.; Halcrow, M. A. The Flexibility of Long Chain Substituents Influences Spin-Crossover in Isomorphous Lipid Bilayer Crystals. *Chem. Commun.* **2021**, *57*, 4039–4042.
- (59) Brooker, S. Spin Crossover with Thermal Hysteresis: Practicalities and Lessons Learnt. *Chem. Soc. Rev.* **2015**, *44*, 2880–2892.
- (60) Miyazaki, Y.; Nakamoto, T.; Ikeuchi, S.; Saito, K.; Inaba, A.; Sorai, M.; Tojo, T.; Atake, T.; Matouzenko, G. S.; Zein, S.; Borshch, S. A. Spin Crossover Phenomenon Accompanying Order-Disorder Phase Transition in the Ligand of [Fe^{II}(DAPP)(abpt)](ClO₄)₂ Compound (DAPP = Bis(3-aminopropyl)(2-pyridylmethyl)amine, abpt = 4-Amino-3,5-bis(pyridin-2-yl)-1,2,4-triazole) and its Successive Self-Grinding Effect. *J. Phys. Chem. B* **2007**, *111*, 12508–12517.
- (61) Weber, B.; Kaps, E. S.; Desplanches, C.; Létard, J.-F. Quenching the Hysteresis in Single Crystals of a 1D Chain Iron(II) Spin Crossover Complex. *Eur. J. Inorg. Chem.* **2008**, 2963–2966.
- (62) J. Laisney, J.; A. Tissot, A.; Molnár, G.; Rechignat, L.; Rivière, E.; Brisset, F.; Bousseksou, A.; Boillot, M.-L. Nanocrystals of Fe(phen)₂(NCS)₂ and the Size-Dependent Spin-Crossover Characteristics. *Dalton Trans.* **2015**, *44*, 17302–17311.
- (63) Siddiqui, S. A.; Domanov, O.; Schafner, E.; Vejpravova, J.; Shiozawa, H. Synthesis and Size-Dependent Spin Crossover of Coordination Polymer [Fe(Htrz)₂(trz)](BF₄). *J. Mater. Chem. C* **2021**, *9*, 1077–1084.
- (64) Gordon, A. J.; Ford, R. A. *The Chemists Companion – A Handbook of Practical Data, Techniques and References*, John Wiley, Chichester, 1972, p. 109.
- (65) Spackman, M. A.; Jayatilaka, D. Hirshfeld Surface Analysis. *CrystEngComm* **2009**, *11*, 19–32.
- (66) Marchivie, M.; Guionneau, P.; Létard, J.-F.; Chasseau, D.; Howard, J. A. K. Thermal Trapped Iron(II) High Spin State Investigated by X-Ray Diffraction. *J. Phys. Chem. Solids* **2004**, *65*, 17–23.
- (67) Craig, G. A.; Costa, J. S.; Teat, S. J.; Roubeau, O.; Yufit, D. S.; Howard, J. A. K.; Aromí, G. Multimetastability in a Spin-Crossover Compound Leading to Different High-Spin-to-Low-Spin Relaxation Dynamics. *Inorg. Chem.* **2013**, *52*, 7203–7209.
- (68) Murnaghan, K. D.; Carbonera, C.; Toupet, L.; Griffin, M.; Dírto, M. M.; Desplanches, C.; Garcia, Y.; Collet, E.; Létard, J.-F.; Morgan, G. G. Spin-State Ordering on One Sub-lattice of a Mononuclear Iron(III) Spin Crossover Complex Exhibiting LIESST and TIESST. *Chem. – Eur. J.* **2014**, *20*, 5613–5618.
- (69) Gómez, V.; Sáenz de Pipaón, C.; Maldonado-Illescas, P.; Waerenborgh, J. C.; Martin, E.; Benet-Buchholz, J.; Galán-Mascarós, J. R. Easy Excited-State Trapping and Record High T_{TIESST} in a Spin-Crossover Polyanionic Fe^{III} Trimer. *J. Am. Chem. Soc.* **2015**, *137*, 11924–11927.
- (70) Weihermüller, J.; Schlamp, S.; Dittrich, B.; Weber, B. Kinetic Trapping Effects in Amphiphilic Iron(II) Spin Crossover Compounds. *Inorg. Chem.* **2019**, *58*, 1278–1289.
- (71) Guionneau, P.; Marchivie, M.; Bravic, G.; Létard, J.-F.; Chasseau, D. Structural Aspects of Spin Crossover. Example of the [Fe^{II}L_n(NCS)₂] Complexes. *Top. Curr. Chem.* **2004**, *234*, 97–128.
- (72) McCusker, J. K.; Rheingold, A. L.; Hendrickson, D. N. Variable-Temperature Studies of Laser-Initiated ⁵T₂ → ¹A₁ Intersystem Crossing in Spin-Crossover Complexes: Empirical Correlations between Activation Parameters and Ligand Structure in a Series of Polypyridyl Ferrous Complexes. *Inorg. Chem.* **1996**, *35*, 2100–2112.
- (73) Marchivie, M.; Guionneau, P.; Létard, J.-F.; Chasseau, D. Photo-Induced Spin-Transition: the Role of the Iron(II) Environment Distortion. *Acta Crystallogr., Sect. B: Struct. Sci.* **2005**, *61*, 25–28.
- (74) Holland, J. M.; McAllister, J. A.; Kilner, C. A.; Thornton-Pett, M.; Bridgeman, A. J.; Halcrow, M. A. Stereochemical Effects on the Spin-State Transition Shown by Salts of [FeL₂]²⁺ [L = 2,6-Di(pyrazol-1-yl)pyridine]. *J. Chem. Soc., Dalton Trans.* **2002**, 2002, 548–554.
- (75) Pask, C. M.; Greatorex, S.; Kulmaczewski, R.; Baldansuren, A.; McInnes, E. J. L.; Bamiduro, F.; Yamada, M.; Yoshinari, N.; Konno, T.; Halcrow, M. A. Elucidating the Structural Chemistry of a Hysteretic Iron(II) Spin-Crossover Compound from its Copper(II) and Zinc(II) Congeners. *Chem. Eur. J.* **2020**, *26*, 4833–4841.
- (76) Kumar, K. S.; Heinrich, B.; Vela, S.; Moreno-Pineda, E.; Bailly, C.; Ruben, M. Bi-Stable Spin-Crossover Characteristics of a Highly Distorted [Fe(1-BPP-COOC₂H₅)₂](ClO₄)₂·CH₃CN Complex. *Dalton Trans.* **2019**, *48*, 3825–3830.
- (77) Kumar, K. S.; Suryadevara, N.; Mizuno, A.; Spieker, L.; Salamon, S.; Sleziona, S.; Maas, A.; Pollmann, E.; Heinrich, B.; Schleberger, M.; Wende, H.; Ruben, M. Structural Insights into Hysteretic Spin-Crossover in a Set of Iron(II)-2,6-Bis(1*H*-pyrazol-1-yl)pyridine Complexes. *Chem. – Eur. J.* **2022**, doi: 10.1002/chem.202103853
- (78) J. Elhaik, J.; Kilner, C. A.; Halcrow, M. A. Insight into Structure:Function Relationships in a Molecular Spin-Crossover Crystal, from a Related Weakly Cooperative Compound. *Eur. J. Inorg. Chem.* **2014**, *2014*, 4250–4253.
- (79) Shongwe, M. S.; Al-Rashdi, B. A.; Adams, H.; Morris, M. J.; Mikuriya, M.; Hearne, G. R. Thermally Induced Two-Step, Two-Site Incomplete ⁶A₁ ↔ ²T₂ Crossover in a Mononuclear Iron(III) Phenolate-Pyridyl Schiff-Base Complex: a Rare Crystallographic Observation of the Coexistence of Pure S = 5/2 and 1/2 Metal Centers in the Asymmetric Unit. *Inorg. Chem.* **2007**, *46*, 9558–9568.
- (80) Tang, J.; Costa, J. S.; Smulders, S.; Molnár, G.; Bousseksou, A.; Teat, S. J.; Li, Y.; van Albada, G. A.; Gamez, P.; Reedijk, J. Two-Step Spin-Transition Iron(III) Compound with a Wide [High Spin-Low Spin] Plateau. *Inorg. Chem.* **2009**, *48*, 2128–2135.
- (81) Phonsri, W.; Harding, D. J.; Harding, P.; Murray, K. S.; Mobaraki, B.; Gass, I. A.; Cashion, J. D.; Jameson, G. N. L.; Adams, H. Stepped Spin Crossover on Fe(III) Halogen Substituted Quinolylsalicylaldehyde Complexes. *Dalton Trans.* **2014**, *43*, 17509–17518.
- (82) Zhu, Y.-Y.; Li, H.-Q.; Ding, Z.-Y.; Lü, X.-J.; Zhao, L.; Meng, Y.-S.; Liu, T.; Gao, S. Spin Transitions in a Series of [Fe(pybox)₂]²⁺ Complexes Modulated by Ligand Structures, Counter Anions, and Solvents. *Inorg. Chem. Front.* **2016**, *3*, 1624–1636.
- (83) Chorazy, S.; Charytanowicz, T.; Pinkowicz, D.; Wang, J.; Nakabayashi, K.; Klimk, S.; Renz, F.; Ohkoshi S.; Sieklucka, B. Octacyanidodihydroxide(V) Ion as an Efficient Linker for Hysteretic Two-Step Iron(II) Spin Crossover Switchable by Temperature, Light, and Pressure. *Angew. Chem. Int. Ed.* **2020**, *59*, 15741–15749.
- (84) Kulmaczewski, R.; Bamiduro, F.; Cespedes, O.; Halcrow, M. A. Gradual Thermal Spin-Crossover Mediated by a Reentrant Z' = 1 → Z' = 6 → Z' = 1 Phase Transition. *Inorg. Chem.* **2017**, *56*, 3144–3148.
- (85) Kobayashi, F.; Komatsumaru, Y.; Akiyoshi, R.; Nakamura, M.; Zhang, Y.; Lindoy, L. F.; Hayami, S. Water Molecule-Induced Reversible Magnetic Switching in a Bis-Terpyridine Cobalt(II) Complex Exhibiting Coexistence of Spin Crossover and Orbital Transition Behaviors. *Inorg. Chem.* **2020**, *59*, 16843–16852.
- (86) Matouzenko, G. S.; Bousseksou, A.; Lecocq, S.; van Koningsbruggen, P. J.; Perrin, M.; Kahn, O.; Collet, A. Polymorphism in Spin Transition Systems. Crystal Structure, Magnetic Properties, and Mössbauer Spectroscopy of Three Polymorphic Modifications of [Fe(DPPA)(NCS)₂] [DPPA = (3-Aminopropyl)bis(2-pyridylmethyl)amine]. *Inorg. Chem.* **1997**, *36*, 5869–5879.
- (87) Buron-Le Cointe, M.; Hébert, J.; Baldé, C.; N. Moisan, N.; L. Toupet, L.; P. Guionneau, P.; Létard, J. F.; Freysz, E.; Cailleau, H.;

Collet, E. Intermolecular Control of Thermoswitching and Photoswitching Phenomena in Two Spin-Crossover Polymorphs. *Phys. Rev. B* **2012**, *85*, 064114.

(88) Tailleur, E.; Marchivie, M.; Negrier, P.; Denux, D.; Massip, S.; Mondieig, D.; Chastanet, G.; Guionneau, P. Using Polymorphism to Master the Spin Crossover Mechanism in $[\text{Fe}(\text{PM-PeA})_2(\text{NCSe})_2]$. *CrystEngComm* **2019**, *21*, 6246–6251.

(89) Vicente, A. I.; Joseph, A.; Ferreira, L. P.; Carvalho, M. D.; Rodrigues, V. H. N.; Duttine, M.; Diogo, H. P.; Minas da Piedade, M. E.; Calhorda, M. J.; Martinho, P. N. Dynamic Spin Interchange in a Tridentate Fe(III) Schiff-Base Compound. *Chem. Sci.* **2016**, *7*, 4251–4258.

(90) Nihei, M.; Tahira, H.; Takahashi, N.; Otake, Y.; Yamamura, Y.; Saito, K.; Oshio, H. Multiple Bistability and Tristability with Dual Spin-State Conversions in $[\text{Fe}(\text{dpp})_2][\text{Ni}(\text{mnt})_2] \cdot \text{MeNO}_2$. *J. Am. Chem. Soc.* **2010**, *132*, 3553–3560.

(91) Buchen, T.; Gülich, P.; Sugiyarto, K. H.; Goodwin, H. A. High-Spin + Low-Spin Relaxation in $[\text{Fe}(\text{bpp})_2](\text{CF}_3\text{SO}_3) \cdot \text{H}_2\text{O}$ After LIESST and Thermal Spin-State Trapping-Dynamics of Spin Transition versus Dynamics of Phase Transition. *Chem. – Eur. J.* **1996**, *2*, 1134–1138.

(92) Floquet, S.; Guillou, N.; Négrier, P.; Rivière, E.; Boillot, M.-L. The Crystallographic Phase Transition for a Ferric Thiosemicarbazone Spin Crossover Complex Studied by X-Ray Powder Diffraction. *New J. Chem.* **2006**, *30*, 621–1627.

(93) Hayami, S.; Hiki, K.; Kawahara, T.; Maeda, Y.; Urakami, D.; Inoue, K.; Ohama, M.; Kawata, S.; Sato, O. Photo-Induced Spin Transition of Iron (III) Compounds with π - π Intermolecular Interactions. *Chem. – Eur. J.* **2009**, *15*, 3497–3508.

(94) Weber, B.; Bauer, W.; Pfaffeneder, T.; Dîrtu, M. M.; Naik, A. D.; Rotaru, A.; Garcia, Y. Influence of Hydrogen Bonding on the Hysteresis Width in Iron(II) Spin-Crossover Complexes. *Eur. J. Inorg. Chem.* **2011**, *2011*, 3193–3206.

(95) Kumar, K. S.; Del Giudice, N.; Heinrich, B.; Douce, L.; Ruben, M. Bistable Spin-Crossover in a New Series of $[\text{Fe}(\text{BPP-R})_2]^{2+}$ (BPP = 2,6-bis(pyrazol-1-yl)pyridine; R = CN) Complexes. *Dalton Trans.* **2020**, *49*, 14258–14267.

(96) (a) Traiche, R.; Sy, M.; Oubouchou, H.; Bouchez, G.; Varret, F.; Boukheddaden, K. Spatiotemporal Observation and Modeling of Remarkable Temperature Scan Rate Effects on the Thermal Hysteresis in a Spin-Crossover Single Crystal. *J. Phys. Chem. C* **2017**, *121*, 11700–11708.

(97) Bushuev, M. B. Kinetics of Spin Crossover with Thermal Hysteresis. *Phys. Chem. Chem. Phys.* **2018**, *20*, 5586–5590.

(98) Capel Berdiell, I.; García-López, V.; Howard, M. J.; Clemente-León, M.; Halcrow, M. A. The Effect of Tether Groups on the Spin States of Iron(II)/Bis[2,6-di(pyrazol-1-yl)pyridine] Complexes. *Dalton Trans.* **2021**, *50*, 7417–7426.